

Chapter 5

Spiral Inertial Microfluidics for Cell Separation and Biomedical Applications



Ning Liu, Chayakorn Petchakup, Hui Min Tay, King Ho Holden Li,
and Han Wei Hou

Abstract The emergence of omics studies and single cell analysis in biomedicine has advocated a critical need to develop novel cell sorting technologies to process complex and heterogenous biological samples prior analysis. Spiral inertial microfluidics is an enabling membrane-free cell separation technique developed almost a decade ago for high throughput biophysical cell separation, and has since been widely exploited for different biomedical applications. In this chapter, we will provide a comprehensive review on spiral inertial microfluidics including (1) conventional and microfluidic cell sorting techniques, (2) introduction to inertial microfluidics and Dean-coupled inertial focusing, (3) classification of major spiral devices, (4) summary of different biomedical applications, (5) recent advances in next generation spiral cell sorters, and (6) highlight key challenges for future research. With increasing advancement in microfabrication and computational simulation, we envision that spiral inertial microfluidics will play a leading role in driving research and commercialization in clinical diagnostics, as well as other research areas in chemistry and material sciences.

Keywords Inertial microfluidics · Cell separation · Biomedical diagnostics

N. Liu · H. M. Tay

Lee Kong Chian School of Medicine, Nanyang Technological University, Singapore, Singapore

C. Petchakup · K. H. H. Li

School of Mechanical and Aerospace Engineering, Nanyang Technological University, Singapore, Singapore

H. W. Hou (✉)

Lee Kong Chian School of Medicine, Nanyang Technological University, Singapore, Singapore

School of Mechanical and Aerospace Engineering, Nanyang Technological University, Singapore, Singapore

e-mail: hwhou@ntu.edu.sg

5.1 Introduction

Cell separation is an essential sample preparation step in biomedical research to purify target cell population and minimize cell-cell interactions prior analysis. For example, subpopulations of cells with unique biological signature and functions are often found in tissue and clinical samples that are highly heterogeneous. It is therefore necessary to isolate specific target cells to facilitate downstream biological assays. Liquid biopsy or blood diagnostic is another important application as blood is routinely obtained during medical checkup, and contains a myriad of information on the health status of an individual. Efficient isolation of blood cell components (white blood cells (WBCs), platelets) or rare diseased cells (cancer or bacteria (~1–100 cells/mL)) from a large cellular background (~5 billion red blood cells (RBCs)/mL) will hence greatly improve signal-to-noise ratio for unbiased and accurate clinical assessment [1].

5.1.1 Conventional Separation Techniques

Conventional “label-free” separation approaches include membrane filtration and centrifugation, which are widely available and simple to use. Membrane filtration works by size-exclusion through a porous matrix which retains cells above a certain size (larger than pore size) and allowing smaller cells to pass through. Target cells can be collected either on the membrane or in the filtrate. Although useful as a pre-enrichment step to remove cell aggregates, clogging issues persist in such systems and it is non-trivial to retrieve the larger target cells from the membrane. Variability in cell deformability can also affect size cut-off or optimal pressure conditions [3, 4]. Differential centrifugation is yet another popular method which separates cells based on size and density, but the isolation of rare cells (< 1000 cells) is not practical and risk substantial cell loss. Furthermore, fluid shear stresses from repeated centrifugation and resuspension can also damage or activate sensitive cells (e.g. neutrophils) [5].

With the growing repertoire of monoclonal antibodies, affinity-based cell separations methods such as fluorescence-activated cell sorting (FACS) and magnetic-activated cell sorting (MACS) have become increasingly popular among biologists. Target cells are first immunolabelled with antibodies which bind to specific surface markers prior separation. FACS relies on fluorophore-conjugated antibodies for separation while MACS employs magnetic microbeads-conjugated antibodies. In FACS, fluorescently-labelled cells are hydrodynamically focused to a narrow stream and passed through a laser beam for signal interrogation. The resulting scatter and fluorescence signals are used to discriminate different cell types based on their cell size, granularity and surface markers. Target cells are subsequently identified based on these biophysical signatures and electrostatically deflected into separate reservoirs for collection [2]. Being a well-established method with high sensitivity and

Table 5.1 Comparison of conventional cell separation techniques

	Separation technique	Principle	Advantages	Disadvantages
Label-free	Filtration	Size	Simple to use	Low purity Low yield Non-specific Requires manual post-processing
	Centrifugation	Density	Relatively cheap	
Affinity-based	FACS	Antibody	High purity	High cost Additional labeling steps May affect cell function
	MACS	Antibody	High yield	
			Highly specific	

throughput, it is often considered as the “gold standard” for cell sorting [3]. A throughput of 2000–10,000 cells per second can be achieved with higher rates sacrificing purity [4]. On the other hand, MACS achieve immuno-magnetic separation by applying an external magnetic field to extract the magnetic bead-bound cells (positive selection) or eluting the non-labelled target cells (negative selection) [5]. In contrast to FACS which enables multiplexed cell sorting, MACS is a bulk and binary processing method, and does not provide individual cell analysis or multi-parametric outputs. Moreover, both methods are usually labor intensive, time-consuming, expensive, and the cell yield or recovery is highly dependent on user operations (Table 5.1).

5.1.2 Microfluidics Cell Separation

With advancement in microfabrication, the birth of microfluidics or lab-on-a-chip technologies since the 1990s has revolutionized chemical analysis and biological assays through unique physical phenomenon and flow control in the microscale [6]. The increasing demand for better and more sensitive assays have propelled the development of many novel microfluidics separation strategies integrated with single cell manipulation and analysis capabilities for point-of-care diagnostics [3, 7, 8]. These miniaturized systems offer numerous advantages including reduced sample and reagent consumption, faster processing time, high spatial resolution, low device cost and high portability [9]. Consequently, microfluidics has become an important toolbox for cell separation applications with the ability to achieve unprecedented size resolution and purity, and high throughput sample processing.

Generally, microfluidic cell separation techniques are classified into active and passive methods based on the involvement of external fields (*e.g.* electric, optical, acoustic, magnetic field) [8, 10, 11]. Active methods exploit external fields to impart different forces on cells to achieve separation, and common examples include magnetophoresis [12–14], dielectrophoresis [15], acoustophoresis [16, 17] and

Table 5.2 Comparison of various passive separation techniques

Separation technique	Mechanism/principle	Separation criteria	Throughput
Biomimetic	Hydrodynamic force/ Fahraeus effect	Size deformability	10 $\mu\text{L/h}$ [19]
Hydrodynamic	Streamline manipulation	Size shape	20 $\mu\text{L/min}$ [20] >10 ⁵ /min [21]
Hydrophoretic filtration	Pressure field gradient	Size	4 $\times 10^3$ /s [22]
Inertial	Lift force secondary flow	Size shape	$\sim 10^6$ /min [23]
Microstructure (Pillars and weirs)	Laminar flow/perturbation of flow	Size deformability	10 ³ $\mu\text{m/s}$ [24] 5 $\mu\text{L/min}$ [25]
Surface affinity	Specific binding to surface markers	Size surface biomarkers	1–2 mL/h [26]
Pinched flow fractionation (PFF)	Laminar flow (Hydrodynamic force)	Size	$\sim 4 \times 10^3$ /min [27] 20 $\mu\text{L/h}$ [27]

optical sorting [18]. Passive separation methods rely on intrinsic hydrodynamic forces during fluid flow which are modulated by microchannel design and flow conditions (Table 5.2).

Numerous efforts have been focused on the development of passive separation methods including deterministic lateral displacement (DLD) [24, 28], pinched flow fractionation (PFF) [27, 29] and inertial focusing/microfluidics. Among these technologies, inertial microfluidics has emerged as a highly promising approach for size-based cell separation due to its ease of operation and high separation resolution. The first seminal work was reported by Di Carlo et al. in 2007 where they described particle inertial focusing effects in microfluidics and its application for high throughput size-based particles/cell separation [30]. This is shortly followed by the Papautsky's group who reported similar particle inertial focusing and Dean migration effects in spiral microchannels [23, 31]. With increasing understanding of the particle inertial focusing behavior [32], many researchers have started working in this exciting field to explore new frontiers and applications in fluid mechanics research and biomedical applications. Unsurprisingly, several review papers on inertial microfluidics have been recently published which give an excellent overview of inertial microfluidics in different channel geometries [33–36]. Spiral microchannel (hereafter termed as spiral inertial microfluidics) is one of the most widely used designs for cell separation as it exploits both size-dependent particle inertial focusing and secondary Dean-induced migration effects to achieve separation. In this chapter, we will first discuss the fundamental principles involved in spiral inertial microfluidics. This is followed by a review of the major types of spiral microfluidics devices and their separation principles. Next, we will provide an overview of spiral cell sorting applications for various bio-entities (cells and molecules) separation, and also highlight recent advances in spiral technologies with novel designs or multiplexing capabilities. Finally, we will conclude with current challenges and suggest future research directions in this area.

5.2 Theory

5.2.1 Stokes Flow

In fluid mechanics, the motion of viscous fluid can be described by the Navier-Stokes equation as shown below:

$$\rho(\partial\mathbf{u}/\partial t + \mathbf{u} \cdot \nabla\mathbf{u}) = -\nabla p + \mu\nabla^2\mathbf{u} + \mathbf{f}$$

where ρ represents the fluid density, μ is the fluid dynamic viscosity, \mathbf{u} is the fluid velocity field, p represents fluid pressure field, and \mathbf{f} is the vector field of external body forces imparting on fluid elements. $\rho(\partial\mathbf{u}/\partial t + \mathbf{u} \cdot \nabla\mathbf{u})$ corresponds to the inertial forces, $-\nabla p$ corresponds to pressures, and $\mu\nabla^2\mathbf{u}$ corresponds to viscous forces.

To characterize fluid flow, the channel Reynolds number (R_c) is proposed as a dimensionless quantity which describes the ratio of inertial to viscous forces:

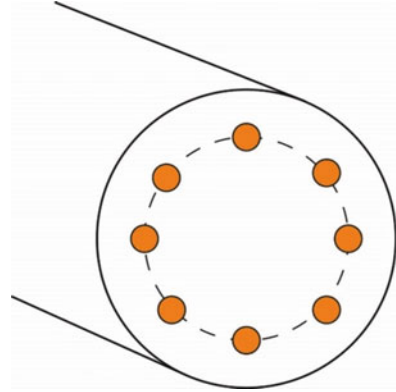
$$R_c = \frac{\rho U_m D_h}{\mu}$$

where ρ represents the fluid density, μ is the dynamic viscosity of the fluid, D_h is defined as the hydraulic diameter where $D_h = d$ in a circular channel (d represents the diameter), or $D_h = 2wh/(w + h)$ in a rectangular channel (w and h denotes the width and height of the rectangular cross section, respectively), and U_m is the maximum velocity of the fluid flow. When considering finite-size particles in the channel flow, the particle Reynolds number (R_p) is helpful to describe the relationship between the particles and the channel dimensions:

$$R_p = R_c \frac{a^2}{D_h^2} = \frac{\rho U_m a^2}{\mu D_h}$$

where a is the particle size. Flow pattern in the channel will change when the size ratio of particle to channel varies. For $R_p \ll 1$, the viscous drag is dominant and the particles are deemed as “point-particle”. As R_p increases, inertial effects become more apparent in the channel flow. Laminar flow occurs when R_c is below a critical value of approximately 2040 [37]. Due to the small channel dimensions (typically less than 1 mm) in microfluidics, R_c is usually less than 100 and fluid flow is completely laminar and the viscous forces of the fluid dominate the inertial forces (Stokes flow). Hence, the inertial portion in Navier-Stokes equation is neglected for most microfluidic systems by equating the left hand side of the equation to zero. Stokes flow lies within laminar regime, but the inverse is not true [33, 34]. Recently, the application potential of the long-ignored intermediate range flow ($\sim 1 < R_c < 100$) has received increasing attention and several inertial-based effects in microfluidics devices include improved mixing and precise particle control [30, 33, 34, 38].

Fig. 5.1 Particle equilibrium positions in a circular straight channel as observed by Segre and Silberberg in 1960s



5.2.2 Inertial Focusing

Segre and Silberberg reported the first observation of particle inertial focusing effects and the earliest interpretation to explain this unintuitive phenomenon in early 1960s [39, 40]. In their experiment, the randomly dispersed particles (~ 1 mm diameter) were introduced into a cylindrical pipe (~ 1 cm diameter). After travelling a distance of 114 cm, the particles were distributed in an annulus between the center and the wall within the cross section of the pipe [40]. The mean radius of the annulus was measured to be ~ 0.6 times the pipe radius, as indicated in Fig. 5.1.

This unique particle lateral migration effect was later found to be the result of the interplay between two dominant inertial lift forces: the shear gradient induced lift force pushing particles in the medium away from the channel center, and the wall induced lift force repelling the particles away from the wall. Another important force to consider is the Stoke's drag force in secondary lateral flow. These forces will be explained in more details below.

5.2.2.1 Wall Induced Lift Force (F_{WL})

For a particle flowing near the channel wall, the interaction between the particle and the wall causes the particle to lag behind the fluid flow. In addition, the constricted flow space between the particle and channel wall will cause the fluid flow at the top side of the particle to be accelerated due to more streamlines diverted toward these side. This creates a relative lower pressure than the "wall side" of the particle and a lift force directed away from the wall is generated (Fig. 5.2a).

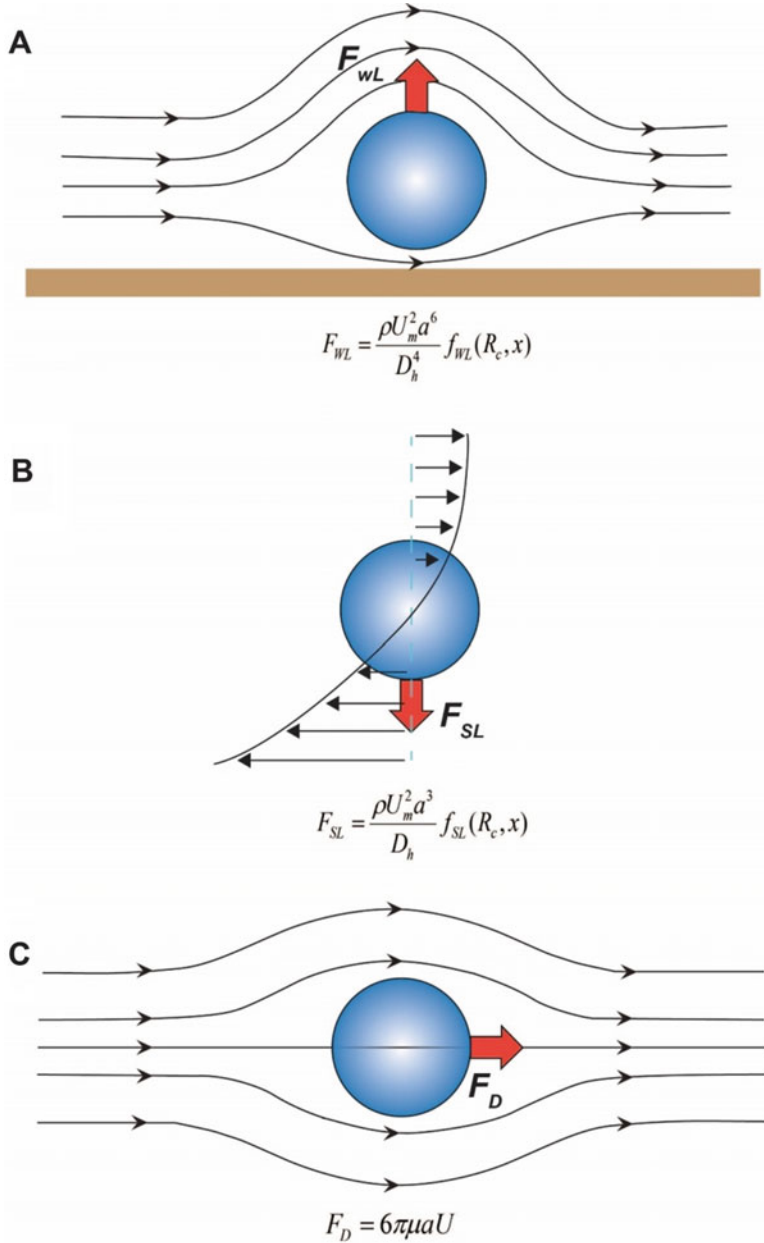


Fig. 5.2 Schematics illustration of the dominant forces experienced by particles in inertial microfluidics (a) Wall induced lift force (F_{wL}), (b) Shear gradient lift force (F_{SL}), (c) Secondary-flow drag force (F_D)

5.2.2.2 Shear Gradient Lift Force (F_{SL})

The shear gradient lift force arises from the curvature of the parabolic velocity profile. As shown in Fig. 5.2b, the velocity magnitudes on each side of the particle are different, leading to a pressure discrepancy between the top and bottom side of the particle. Due to the existence of the pressure difference, a shear gradient lift force is exerted on the particle which pushes it towards the channel wall (until it is balanced by the wall induced lift force).

5.2.2.3 Net Lift Force (F_L)

Following the discovery by Segre and Silberberg, matched asymptotic expansion methods were proposed to determine the lateral lift forces acting on particles during flow. Asmolov derived an analytical expression of the net lift force imparting on a rigid particle ($a/D_h \ll 1$) in a Poiseuille flow [41]:

$$F_L = \frac{\rho U_m^2 a^4}{D_h^2} f(R_c, x) = \frac{\mu^2}{\rho} R_p^2 f(R_c, x)$$

where $f(R_c, x)$ is the lift coefficient which depends on the particle position within the channel (x) and the channel Reynolds number (R_c).

Conventional theoretical predications are based on “point-particle” approximation which neglects the size effect of particles. However, when the particle size approaches the channel dimension, the disturbance to the flow will be affected by the particles. Di Carlo et al. experimentally demonstrated that the net lift force varies with the position in the microchannel [32]. For a particle of finite-size ($0.05 \leq a/D_h \leq 0.2$), the lift force scaling relationship is modified as: $F_{WL} = \frac{\rho U_m^2 a^6}{D_h^4} f_{WL}(R_c, x)$ near the channel wall, and as $F_{SL} = \frac{\rho U_m^2 a^3}{D_h} f_{SL}(R_c, x)$ near the channel center. The variation of lift forms is attributed to the disparate fluid dynamics in different positions of the channel. Near the center of the channel, the shear gradient lift force dominates, while the wall induced lift force is more significant near the channel wall.

5.2.2.4 Secondary-Flow Drag Force

Besides the wall induced lift force (F_{WL}) and the shear gradient induced lift force (F_{SL}), the secondary-flow drag force is the third major force responsible for particle inertial migration and focusing effects. In 1928, William Dean reported the presence of Dean vortices in curved channels due to the mismatch of fluid momentum within the channel cross section as a result of the centrifugal acceleration acting on the fluid flow [42]. Briefly, when fluid flows through a curved channel, the fluid velocity at

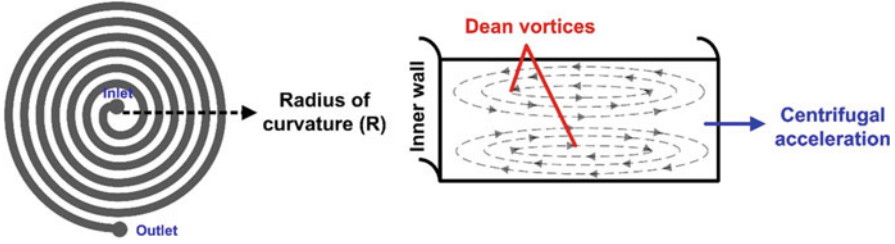


Fig. 5.3 Schematic of a pair of Dean vortices within a spiral channel with a rectangular cross section

the center of the channel is higher than the sides due to the parabolic flow profile. This introduces an additional momentum to the faster-moving fluid in the channel center, and is pushed toward the outer wall (the concave wall) of the channel curvature along the channel midline due to centrifugal acceleration. By conservation of mass, secondary counter-rotating flows are induced to compensate the fluid shifting. Hence, two symmetrical counter-rotating vortices are formed at the top and the bottom of the cross-sectional plane (Fig. 5.3). Hereafter, the terms Dean flow and secondary flow are used interchangeably [35].

The strength of the secondary flow can be characterized by a non-dimensional Dean number (De):

$$De = R_c \sqrt{\frac{D_h}{2R}}$$

where R_c is the channel Reynolds number defined as $R_c = \rho U_m D_h / \mu$, here U_m is the maximum channel velocity, μ and ρ is the dynamic viscosity and density of the fluid, respectively. The curvature ratio ($\delta = D_h / 2R$, where R is the average radius of curvature of the channel) implies a faster turn in the channel (*i.e.* smaller radius of curvature R) and results in a stronger Dean flow.

For a given De , the expression of average transverse Dean velocity can be determined by [43]:

$$U_{De} = 1.84 \times 10^{-4} De^{1.63} \text{ (m/s)}$$

Accordingly, the Dean drag force experienced by a particle located in this flow can be derived by assuming Stokes drag (Fig. 5.2c) and is expressed as:

$$F_D = 3\pi\mu U_{De} a = 5.4 \times 10^{-4} \pi\mu De^{1.63} a \text{ (N)}$$

In spiral or curvilinear channels, the interplay of the net inertial lift force (F_L) and Dean drag force (F_D) gives rise to the Dean coupled inertial migration of particles. To characterize particle inertial focusing in curved channel, Di Carlo et al. proposed

a key parameter R_f , the ratio of shear gradient lift force to Dean drag force, to describe the behavior [35, 44]:

$$R_f = \frac{F_{SL}}{F_D} \propto \frac{1}{\delta} \frac{a^2}{D_h^3}$$

It is well accepted that $R_f > 0.04$ (or $a/D_h > 0.07$ [23]) to achieve particle inertial focusing in microchannels. As R_f has a strong dependence on particle size ($\sim a^2$), this forms the basis for size-based particle separation in spiral devices since the particle equilibrium separation can be modulated by tuning these forces. This is explained in more details in the following section.

5.2.2.5 Dynamics of Particle Lateral Migration in Spiral Microchannel

Figure 5.4 depicts the schematic illustration of particle focusing dynamics in a low-aspect ratio spiral microchannel. Due to the asymmetrical parabolic flow profile,

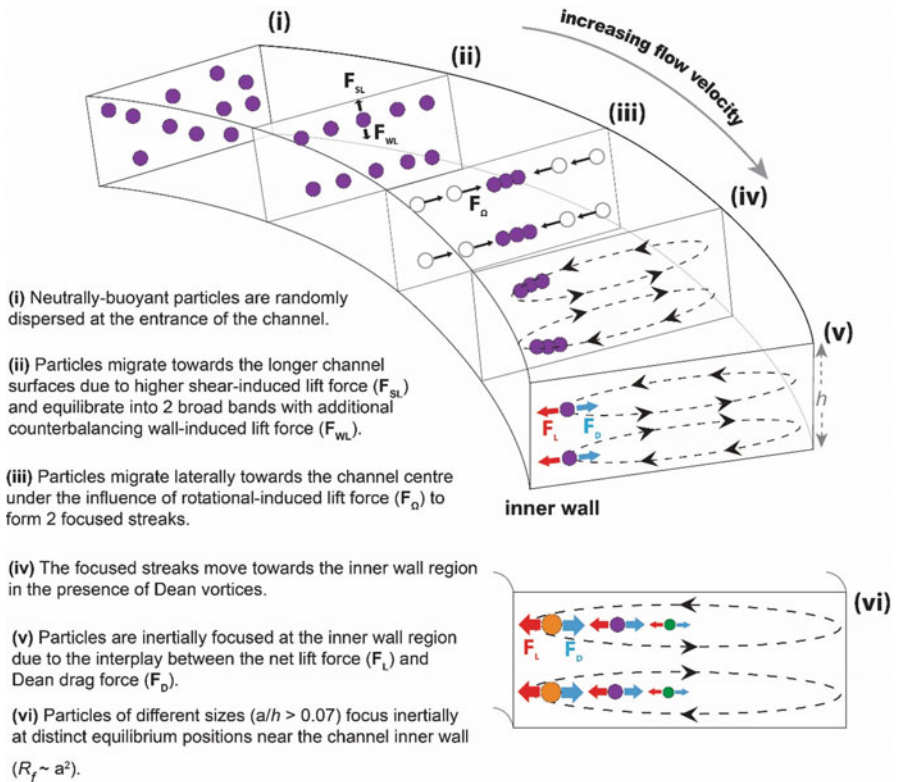


Fig. 5.4 Schematic illustration of particle migration dynamics in spiral microchannels

a steep shear gradient is generated along the vertical direction (height) of the channel. The randomly distributed particles (1) are first pushed by dominant shear gradient lift force (F_{SL}) across streamlines towards the channel top and bottom surfaces. Near the wall, the particles experience opposing wall-induced lift force (F_{WL}) and equilibrate into two broad bands at $\sim 20\%$ of channel height from surface (2). Next, a rotational-induced lift force (F_{Ω}), first proposed by Saffman [45], will act on the particles and they begin to migrate laterally towards the centre face of the channel wall to form two focused streaks (3). This lift force F_{Ω} is usually considered negligible compared with other lift forces (an order of magnitude lower than F_{WL} and F_{SL}), but becomes important in radially-asymmetric (e.g. rectangular) channels as particles exhibit spinning behavior in the presence of high (localized) shear rate close to the channel wall [46]. Other groups have reported the particle size dependency of F_{Ω} ($F_{\Omega} \sim a^3$) [47], and this effect is also recently used by Zhou et al. for particle separation in straight channels [48, 49]. With increasing flow velocity, the strength of the secondary Dean drag force becomes more significant and particles begin to migrate towards the inner wall region in the direction of the Dean vortices (4). Finally, a single focusing point is achieved near the inner wall region in each Dean vortice as a result of the balance of net inertial lift force (F_L) and Dean drag force (F_D) (5). As this equilibrium position is strongly dependent on particle size ($R \sim a^2$), larger particles ($a/h > 0.07$, as $D_h \approx h$ in a low aspect ratio channel[50]) will focus closer to the inner wall due to stronger inertial lift ($F_L \sim a^3$ vs. $F_D \sim a$) while smaller particles are positioned further away from inner wall [23] (6). For all particle sizes, a further increase in flow velocity will shift the focused particle streams back towards the outer wall due to increasing F_D [51]. Although an increase in flow velocity results in a greater lift force ($F_L \sim U_m^2$) as compared to the Dean drag ($F_D \sim U_m^{1.63}$), the particle movement away from the inner wall can be explained by a decrease in the lift coefficient $f(R_c, x)$ which is dependent on particle position within the channel [23].

5.3 Classification of Spiral Devices

Fluid mixing at the microscale poses a variety of challenges due to the dominant viscous drag forces (low Re), and molecular diffusion remains the main transport mechanism in this laminar flow regime. By taking advantage of the transverse Dean vortices in curvilinear channels, spiral microdevices have been used as micromixer to enhance fluid mixing [52, 53], and rotate cells in electroporation systems for efficient gene delivery [54]. Since flow conditions and channel geometries can affect the shape and magnitude of Dean vortices, these parameters have been extensively investigated in spiral inertial microfluidics to enhance cell sorting capabilities. In this section, we will describe four major types of spiral devices with different cells/particles focusing mechanisms and features: (1) rectangular spiral microfluidics, (2) trapezoidal spiral microfluidics, (3) double-inlet spiral termed as Dean Flow Fractionation (DFF), and (4) High-resolution Dean Flow Fractionation (HiDFF).

5.3.1 Rectangular Spiral Microfluidics

Spiral microchannels with rectangular cross-section are one of the most widely used geometry, due to the well-established microfabrication techniques (photolithography and deep reactive ion etching (DRIE)) which can generate uniform channel/feature height and high aspect ratio vertical sidewall. The small feature size resolution ($\sim 1\text{--}10\ \mu\text{m}$) in microfabrication also enables the design of complicated outlet bifurcations (8–15 outlets) for multiplexed separation. In low-aspect ratio rectangular spiral channels, the regular cross-section geometry will lead to the formation of symmetrical Dean vortices along the channel midline. Inertial forces are weaker across the longer dimension (due to the blunting of the velocity profile) and particles will first migrate along the shorter channel dimensions (channel height) to the top and bottom surfaces due to higher shear rate [50]. Once particles have reached the z-direction equilibrium positions, they will then migrate along the channel width to the final equilibrium position near the inner wall region. Martel and Toner have performed a systematic characterization of inertial focusing dynamics in spiral microchannels of varying widths (Fig. 5.5a). Generally, as channel dimensions (D_h) increase, particles experience less shear-induced inertial forces (blunting of velocity profile) and more Dean drag force ($\sim D_h^{1.5}$). They proposed slight modifications to R_f (ratio of F_L/F_D) by using $U_{\text{Dean, ave}}$ in the equation to reduce variability of R_f to ~ 1 for quality focusing in different spiral designs [55]. A straightened composite image was also generated from empirically-determined particle focusing images to more clearly visualize the particle focusing streak width and position along the entire channel length (Fig. 5.5b).

As described previously, the interplay between inertial lift (F_L) and Dean drag forces (F_D) is important to focus particles of different sizes at distinct equilibrium positions. Early work by Kuntaegowdanahalli et al. [23] and Russom et al. [56] clearly demonstrated the capability of spiral microchannels for continuous high throughput size-based particle separation into different outlets. As shown on Fig. 5.6a, large particles ($a/h > 0.07$) focused inertially close to the channel inner wall due to dominant F_L . At high flow conditions ($De \sim 10\text{--}15$, $\sim 3\ \text{mL/min}$), significant Dean drag force would move these focused streams farther away from the channel inner wall based on particle size, with the largest particles being closest to the inner channel wall. This phenomenon was exploited to separate closely-spaced microparticles ($10\ \mu\text{m}$, $15\ \mu\text{m}$, $20\ \mu\text{m}$) in a $500\ \mu\text{m}$ wide Archimedean spiral device ($130\ \mu\text{m}$ height) [23]. Xiang et al. also developed a smaller spiral device ($160\ \mu\text{m}$ width, $50\ \mu\text{m}$ height) for binary separation of $4.8\ \mu\text{m}$ and $2.1\ \mu\text{m}$ particles Fig. 5.6b [57]. In addition, they also described the non-focusing behavior of smaller $2.1\ \mu\text{m}$ particles ($a/D_h \ll 0.07$) and the resultant particle-free regions at low flow conditions ($De \sim 1\text{--}5$). Besides particle sorting and filtration applications, inertially-focused particle stream in rectangular spiral channels is used for cell self-ordering for deterministic single-cell droplet encapsulation [58]. Noteworthy, the above mentioned Dean-coupled particle inertial focusing effects can also be applied in other curvilinear channels with symmetrical cross section geometry including double

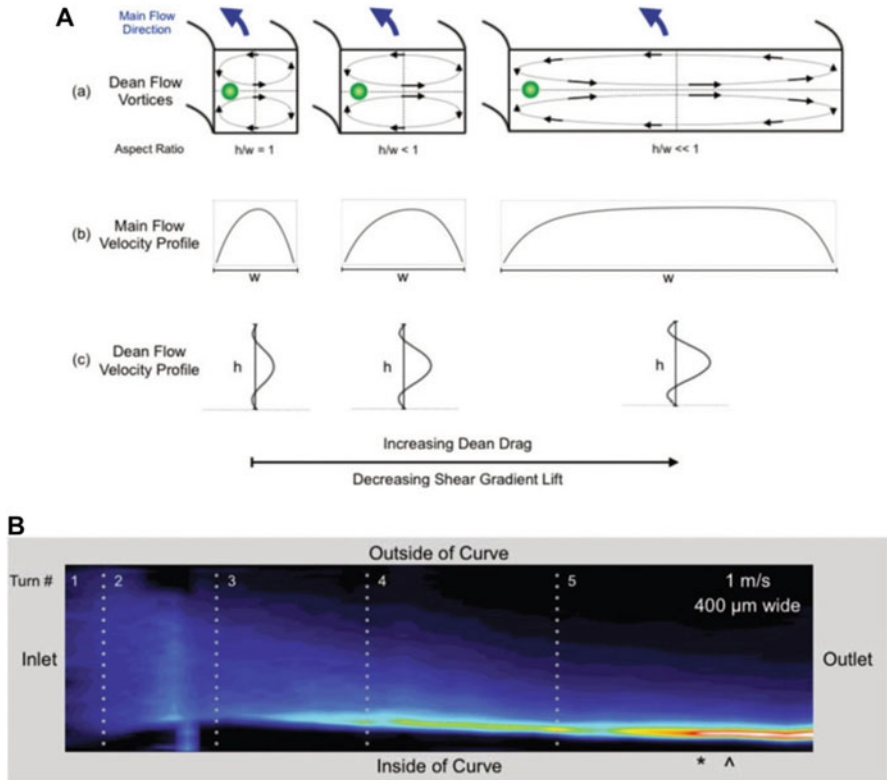


Fig. 5.5 Rectangular spiral microfluidics (a) Schematic illustrations of different flow profiles and associated forces in curved channels of different widths, (b) Straightened image of the inertial focusing behavior of $15 \mu\text{m}$ beads in a spiral channel. Dotted lines represent channel curvature changes. (Reproduced with permission from Ref. [55])

spiral [59–61], serpentine [30], as well as soft microtubes (circular cross section) coiled in planar or 3D spiral (helical) [62].

Recently, Nivedita et al. performed experimental and numerical simulation studies on fluid flow dynamics in spiral microchannels under high flow conditions. They reported the presence of multiple pairs of secondary flow vortices at high Re (>100) and De (~ 20 – 40), and defined a non-dimensional parameter termed as critical Dean number (De_c) to describe this novel flow observations [63]. According to them, the formation of additional Dean vortices was due to the large pressure gradient between the high velocity area and the channel outer wall. Above De_c , the primary Dean vortices were unable to maintain the pressure across the channel width. In order to balance the pressure, the primary vortices would thus split to recirculate the fluid near the outer wall region. This led to the formation of secondary Dean vortices which can entrain particles or cells at higher flow rates (Fig. 5.6c).

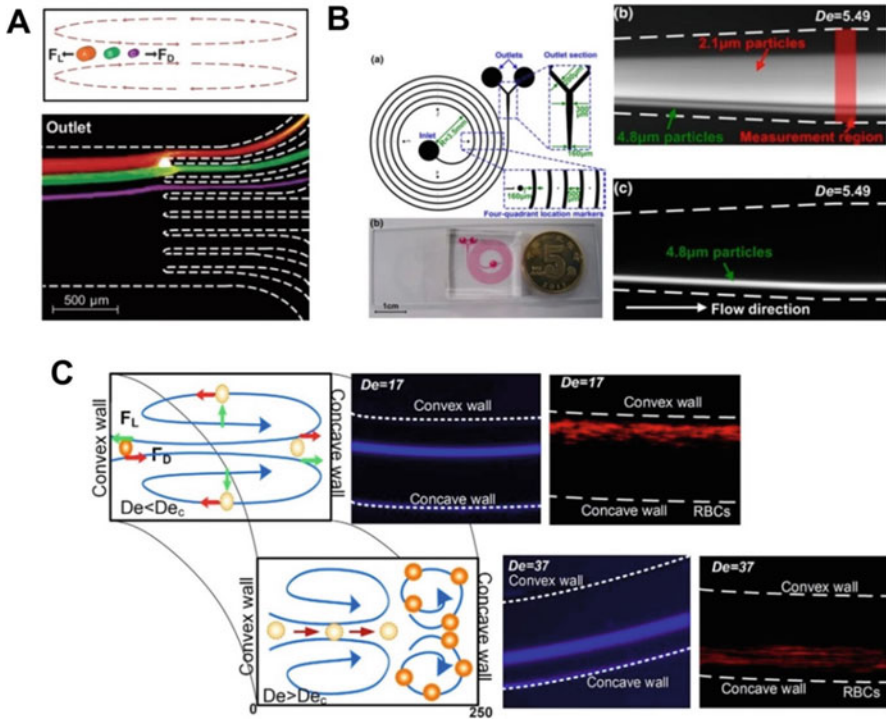


Fig. 5.6 Rectangular spiral microfluidics (a) Schematic illustration and fluorescence image indicating multiplexed separation of 10 μm , 15 μm , 20 μm microparticles into different outlets in a 500 μm wide and 130 μm tall Archimedean spiral device. (Reproduced from Ref. [23] with permission from The Royal Society of Chemistry) (b) CAD design and optical image of a 5-loop spiral device (filled with red dye) fabricated in polydimethylsiloxane (PDMS). Fluorescent images indicating tight focusing of 4.8 μm particles near the inner wall and the wider 2.1 μm particles band at the channel centre. (Reproduced with permission from Ref. [57].) c Schematic and fluorescent images of 10 μm particles (blue) and RBCs (red) entrapment in additional Dean vortices at high De (~ 37). (Reproduced from Ref. [63] under Creative Commons)

5.3.2 Trapezoidal Spiral Microfluidics

Intuitively, one can modulate the Dean vortices to increase the separation distance between particles of different sizes and enhance the separation resolution. Trapezoidal cross section is an interesting design as the change in channel height from low (inner wall) to high (outer wall) results in a Dean flow velocity gradient across the channel width. Guan et al. first reported this behavior, and found that the skewed Dean vortices were beneficial for particles separation as the gradient in F_D across the channel would lead to a sharp transition of size-based focusing behavior beyond a certain threshold flow rate [64]. Unlike in rectangular spiral channels where focused particles streams gradually migrate towards the outer wall with increasing flow rates,

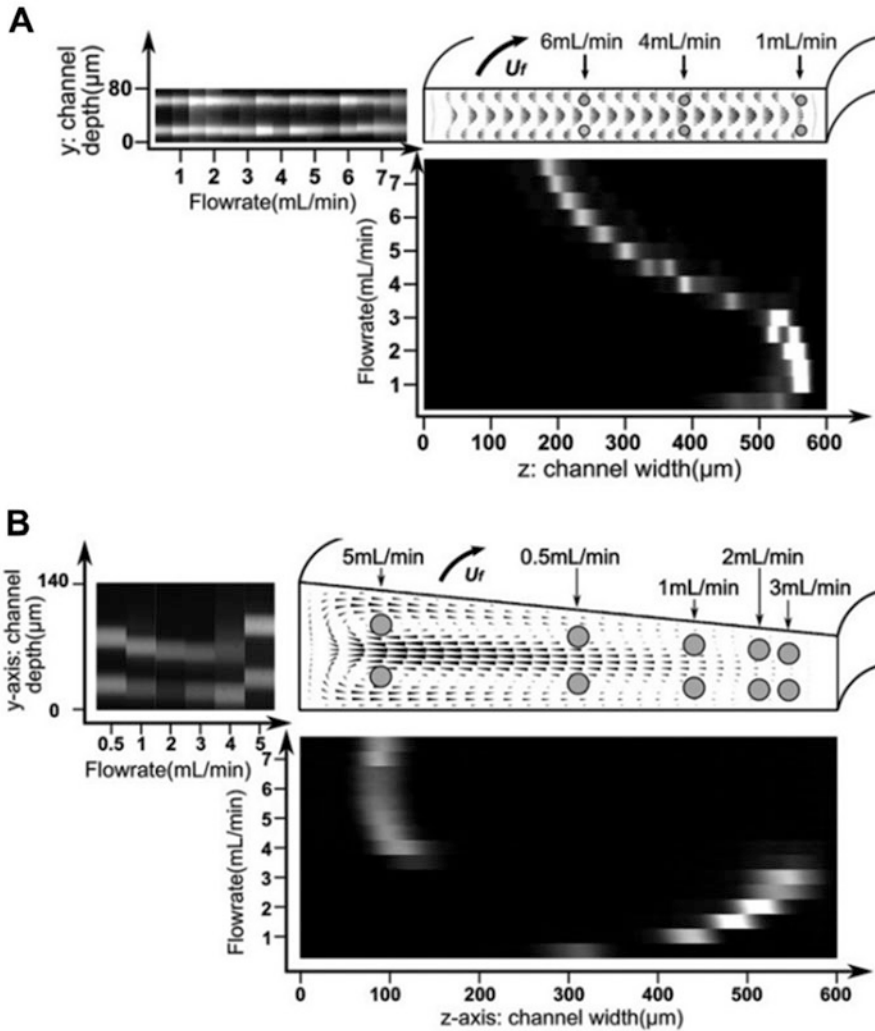


Fig. 5.7 Comparison of rectangular and trapezoidal spiral microchannels. CFD simulation and experimental results (*top and side view*) of (a) 15.5 μm particles focusing behavior in rectangular spiral microchannel (600 μm width, 80 μm height) and (b) 26.25 μm particles focusing behavior in trapezoidal spiral microchannels (600 μm width, 80–140 μm height). (Reproduced with permission from Ref. [64])

focused particles in trapezoidal spiral channels would “switch” to an equilibrium position located at the outer half (deeper side) of the channel as flow rate increases (Fig. 5.7). Side view analysis also revealed that these particles were trapped within the Dean vortices at the outer wall region [64].

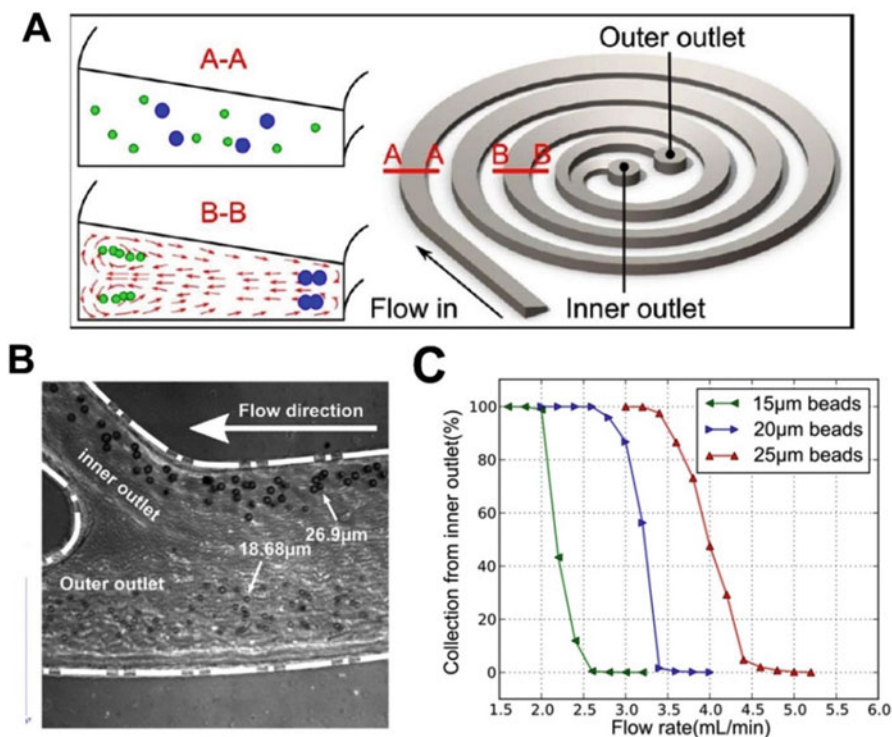


Fig. 5.8 Binary particle separation in trapezoidal spiral microchannels (a) Schematic illustration of particle focusing and trapping within the skewed Dean vortices in trapezoidal cross-section spiral microchannel (b) High speed image at the outlet bifurcation showing separation of 18.68 μm and 26.9 μm particles (*channel dimensions: 600 μm width, 80–140 μm height*) (c) Flow rate characterization of size-based “threshold” flow rate to switch particles focusing to outer wall focusing. (Reproduced with permission from Ref. [64])

As the threshold flow rate is a function of particle size, this novel focusing behavior was used to achieve efficient binary separation ($\sim 92\text{--}96\%$) of particle mixtures in a 2-outlet trapezoidal spiral channel (Fig. 5.8). This is ideal as one can process samples at high throughput ($\sim 3\text{--}4$ mL/min) and higher particle concentrations ($\sim 10^7/\text{mL}$) by minimizing the interactions between particles of different sizes. This method was applied for separation of leukocytes ($\sim 10\text{--}15$ μm) [65] and circulating tumor cells (CTCs) ($\sim 15\text{--}20$ μm) [66] from blood samples (RBCs $\sim 6\text{--}8$ μm), as well as macroscale filtration (~ 500 mL/min) of Chinese hamster ovary (CHO) and yeast cells in bioprocessing [67]. However, a major limitation of trapezoidal spiral microchannels is the use of micromilling [64] or 3D printing [68] techniques to fabricate the channel molds with uneven channel heights. Due to the relatively poor feature size resolution as compared to conventional microfabrication, the devices are limited to a 2-outlet bifurcation and thus only used for binary separation.

5.3.3 Double-Inlet Spiral/ Dean Flow Fractionation (DFF)

Rectangular and trapezoidal spiral microchannels are highly effective for size-based particle and cell separation with working sample concentrations of $\sim 10^{5-7}$ /mL, but their use in blood-related applications is greatly limited by the large RBCs background ($\sim 45\%$ v/v, $\sim 10^9$ RBCs/mL) as RBCs-RBCs interactions can severely affect the cell focusing behavior and hence deteriorate separation efficiency [69]. Typically, whole blood samples have to be diluted significantly ($50\text{--}100\times$, $\sim 0.1\text{--}2\%$ hematocrit) which increases the processing time, making them unsuitable to process large volumes of blood samples required in clinical settings.

In a landmark work by Bhagat et al. [31], they developed a 2-inlet spiral channel to selectively introduce particle samples on the inner side of the channel with an additional sheath flow. As the particles flow through the spiral device ($100 \times 50 \mu\text{m}$ ($w \times h$)), the Dean vortices would transpose the smaller particles ($a/D_h < 0.07$) towards the outer wall, and both inertial lift and Dean drag forces would equilibrate the larger particles ($a/D_h > 0.07$) near the inner wall. This was used for complete separation of $1.9 \mu\text{m}$ and $7.32 \mu\text{m}$ particles at $De = 0.47$ (Fig. 5.9a). It should be noted that unlike in 1-inlet rectangular spiral channels where all particles are inertially focused near the inner wall and their final equilibrium positions differ slightly based on size differences, the $1.9 \mu\text{m}$ particles did not undergo inertial focusing effects in the dual-inlet spiral device and solely migrated to the outer wall under the influence of Dean vortices. This was the primary reason for the significantly wider $1.9 \mu\text{m}$ particles focusing band as compared to $7.32 \mu\text{m}$ particles (Fig. 5.9a).

Inspired by this work, Hou et al. subsequently developed a 2-inlet 2-outlet spiral device ($500 \mu\text{m}$ (w) \times $160 \mu\text{m}$ (h)) for isolation of CTCs from whole blood, aptly termed as Dean Flow Fractionation (DFF) [70] (Fig. 5.9b). Based on the size difference between CTCs and blood cells [71, 72], the developed technique enables inertial focusing of larger CTCs ($15\text{--}20 \mu\text{m}$) near the inner wall while smaller blood components (RBC $\sim 8 \mu\text{m}$ discoid; leukocytes $\sim 7\text{--}12 \mu\text{m}$) are solely affected by the Dean drag and transposed towards the outer wall, thus achieving separation. The authors further define this Dean-induced lateral migration in terms of ‘Dean cycle’ (DC) which can be modeled by COMSOL simulation (Fig. 5.9b). For instance, a particle which is initially positioned near the microchannel outer wall and migrates to the inner wall is said to have completed $\frac{1}{2}$ Dean cycle (DC 0.5), and returning back to the original position near the channel outer wall completes a full Dean cycle (DC 1). The length for a complete Dean cycle migration (L_{DC}) can be approximated as $L_{DC} \sim 2w + h$ (where w is the microchannel width and h is the channel height). For a given microchannel length, the particles can thus undergo multiple DC migration with increasing flow rate conditions (Fig. 5.9b).

Notably, this separation principle is particularly useful for blood cell separation as the additional sheath buffer in DFF device facilitates the Dean migration of large volume of RBCs in a well-controlled manner. The authors reported that RBCs band broadened with increasing hematocrit due to cell-cell interaction induced dispersion

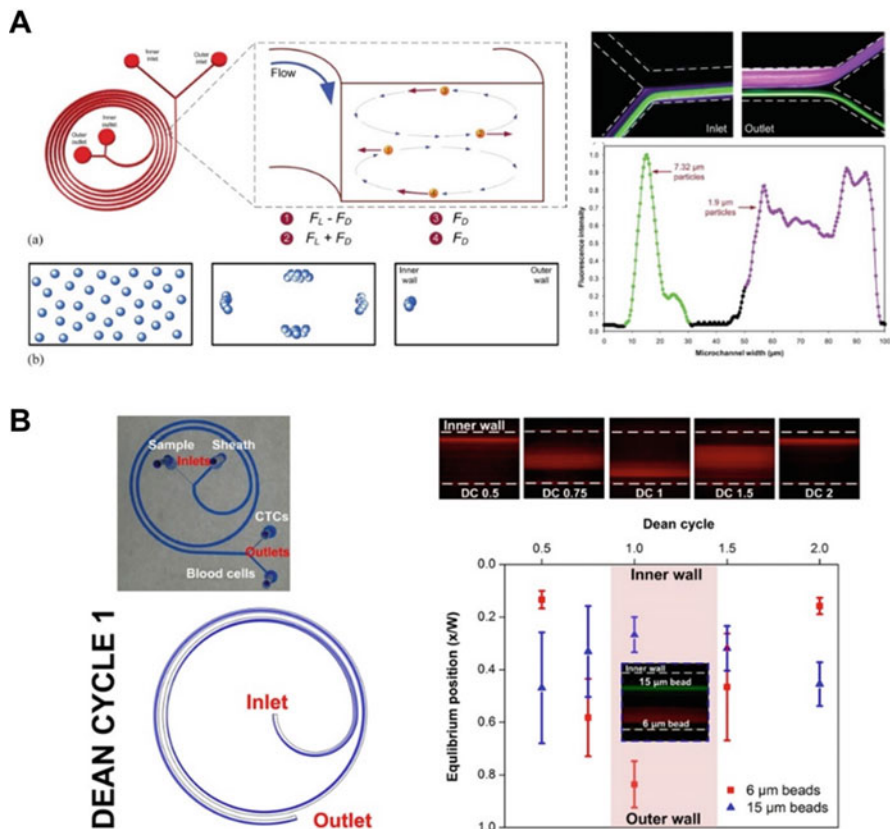


Fig. 5.9 Dean Flow Fractionation (DFF) using a 2-inlet spiral design (a) (left) Schematic illustration of the Dean-coupled inertial focusing separation principle in the 2-inlet spiral device. (right) Composite fluorescent images and intensity line scans illustrating complete separation of 1.9 μm (purple) and 7.32 μm (green) particles at $De = 0.47$. (Reproduced from Ref. [31] with permission from The Royal Society of Chemistry) (b) (left) Optical image of the DFF spiral microchannel (filled with blue dye for visualization) used for CTCs isolation from whole blood. Fluid simulation and particle tracking (blue streamlines) in the DFF spiral device at Re 50 (DC 1) indicating complete recirculation of the fluid elements at the outer wall region (inlet) and back to the outer wall (outlet) again. (right) Average composite fluorescence images and plot indicating equilibrium position of 6 μm and 15 μm beads at different DC . (Reproduced with permission from Ref. [70])

and a final hematocrit of 20% was chosen as it resulted in negligible RBCs contamination in the inner CTCs outlet (Fig. 5.10a). Compared to other inertial-based microfluidic separation methods, 20% hematocrit implies $\sim 2\times$ dilution of whole blood (original hematocrit $\sim 40\text{--}45\%$). This translates to an unprecedented processing time of ~ 20 minutes for 1 mL of whole blood (at 100 $\mu\text{L}/\text{min}$). Interestingly, inertial focusing positions of cancer cells (MCF-7) remained similar in saline solution and 20% hematocrit blood samples, indicating that the lateral migration of RBCs did not affect their inertial focusing (Fig. 5.10b) [70]. The same group later

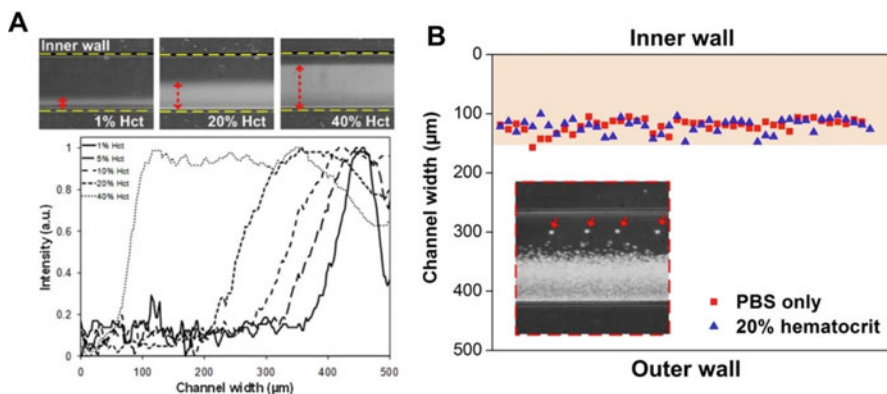


Fig. 5.10 High blood sample concentration processing in DFF (a) Averaged composite images and intensity plot illustrate broadening of RBCs occupied regions (*red dashed line*) for increasing hematocrit prior outlet bifurcation. *Yellow dotted lines* indicate position of channel walls, (b) Plot and high speed image captured at the channel outlet (*red dotted box*) indicate similar focusing positions of MCF-7 cancer cells suspended in PBS solution and 20% hematocrit blood samples at DC 1. *Shaded area* (150 μm wide) corresponds to the dimension of CTCs outlet. (Reproduced with permission from Ref. [70])

applied the DFF technology for label-free isolation of rare bacteria from whole blood by collecting the Dean-induced migrated bacteria at the channel outer wall [73].

Compared to other spiral technologies, DFF is clearly more versatile as it can achieve both size-dependent differential inertial focusing and multiplexed sorting of larger particles, as well as isolation of smaller micro or nanometer-sized elements through well-controlled Dean migration (a feat not possible with rectangular or trapezoidal spiral microchannels). Figure 5.11 illustrates the Dean migration profiles of 50 nm particles along the channel in DFF devices when introduced at either the inner or outer inlet. In both cases, the particles are solely affected by the Dean drag and migrated in the directions of the Dean vortices. By carefully tuning the sample to sheath flow rate ratio, DFF could thus serve as an efficient buffer exchange system to deplete smaller biological components including biomolecules (aptamers) [74] and nanoparticles [75] from target cells with high efficacy.

5.3.4 High-Resolution Dean Flow Fractionation (HiDFF)

In biomedical research, there exists a critical need to develop novel separation tools for sub-micron components in particle-based drug delivery system and purification of circulating microvesicles. While DFF enables well-controlled, Dean-induced migration of small microparticles (biomolecules, bacteria *etc.*) from inertially-focused larger target cells, a major drawback remains in its inability to further size-fractionate smaller microparticles (*e.g.* 1 μm vs. 2 μm) as they recirculate

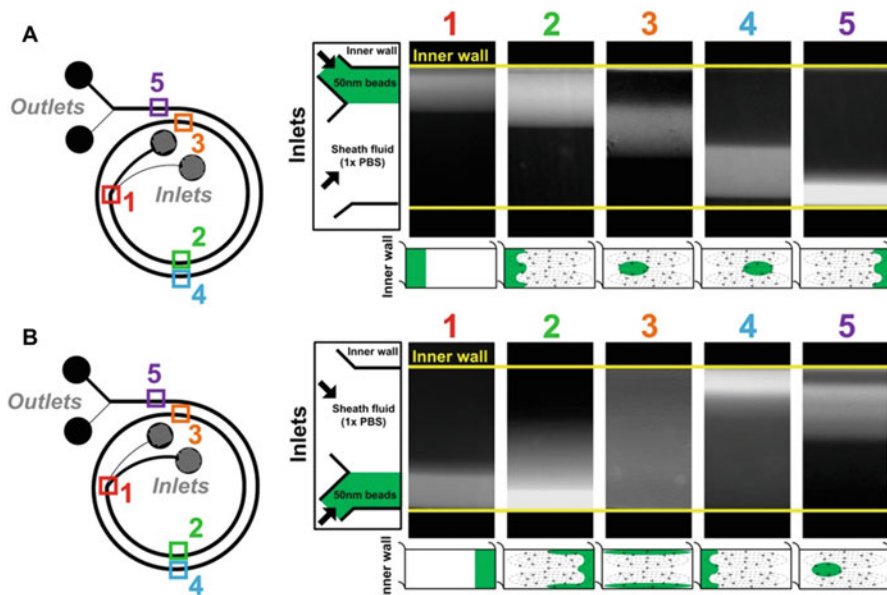


Fig. 5.11 Characterization of Dean-induced lateral migration of nanoparticles in DFF spiral devices. 50 nm fluorescent bead sample is introduced at the **a** inner wall or **b** outer wall at the inlet region. Average fluorescent stacked images indicate 50 nm bead positions along the channel. *Yellow lines* indicate positions of channel wall. Corresponding schematic images of channel cross section illustrate differences in bead migration pattern depending on initial position of beads. (Reproduced from Ref. [76] under Creative Commons)

continuously due to Dean vortices. Inertial focusing of small particles is highly challenging due to the requirement for smaller channel geometries ($a/h > 0.07$; $D_h \leq \sim 10 \mu\text{m}$ for $1 \mu\text{m}$ bead focusing), and the large channel resistance would cause flow-induced channel deformation [77]. A spiral sorter was developed to inertially focus 2.1 and 3.2 μm microparticles, but the operating flow rate was low (10 $\mu\text{L}/\text{min}$) due to large pressure drop [78].

To address these limitations, the Hou group recently developed a novel 2-inlet, 2-outlet spiral sorting technology termed as High-resolution DFF (HiDFF) [76]. Contrary to current inertial microfluidics technologies, this was based on a novel phenomenon in spiral inertial microfluidics where particle transient innermost distance (D_{inner}) varied with size during Dean vortices-induced migration (Fig. 5.12a). Briefly, small microparticles ($a/D_h < 0.07$) introduced at channel outer wall experience Dean drag forces (F_D) due to Dean vortices and migrate laterally towards inner wall. As they migrate along the channel top or bottom, particles near the surface experience size-dependent wall-induced inertial lift forces ($F_{\text{WL}} \propto a^6$) that push particles away from the surface. Hence, particles flow at different fluid streamlines which leads to a differential transient innermost position (D_{inner}) at the inner wall before they recirculate back towards the outer wall (Fig. 5.12b). Of note, since

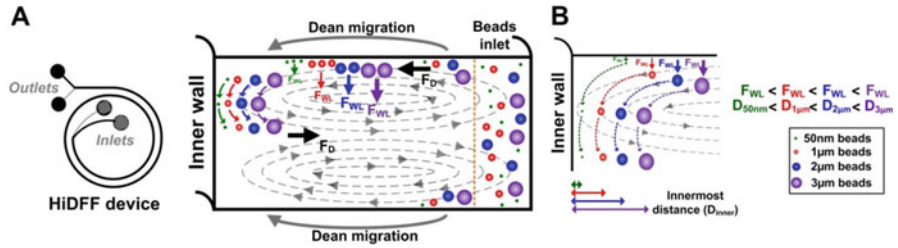


Fig. 5.12 High-resolution Dean Flow Fractionation (HiDFF) (a) Schematic illustration of HiDFF separation principle in a 2-inlet, 2-outlet spiral ($300\ \mu\text{m}$ (w) \times $60\ \mu\text{m}$ (h)) device. Particles introduced at the outer wall migrate laterally towards inner wall under the influence of Dean vortices. As the particles migrate along the channel top and bottom, they experience size-dependent wall-induced lift forces (F_{WL}) that push larger particles away from the surfaces, (b) Subtle differences in particle z-position (along height) lead to size-based transient innermost distance (D_{inner}) at the inner wall which can be exploited for small particle separation. (Reproduced from Ref. [76] under Creative Commons)

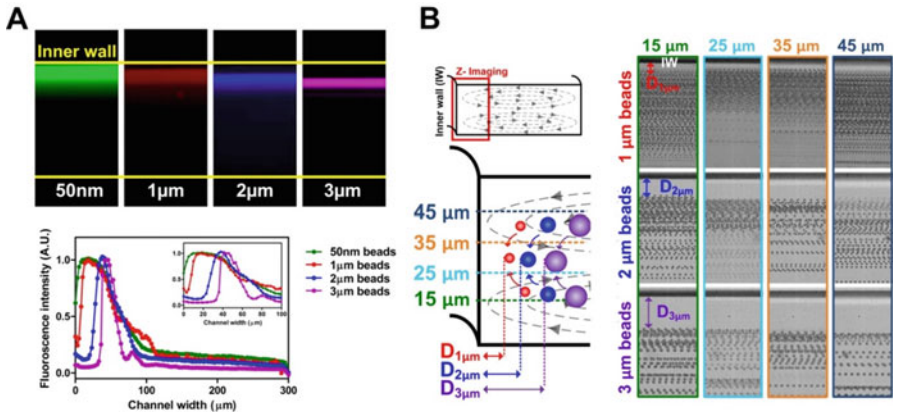


Fig. 5.13 Superior separation resolution of HiDFF (a) Fluorescence composite images and intensity line scans indicating distinct innermost distance (D_{inner}) for particles of different sizes (b) High speed, Z-imaging ($40\times$ magnification) of inner wall region at different planes indicates similar D_{inner} along channel height. (Reproduced with permission from Ref. [76])

inertial focusing of particles is not necessary, channel dimensions are increased to minimize clogging while improving throughput significantly ($\sim 100\ \mu\text{L}/\text{min}$).

To characterize the dependence of D_{inner} with particle size, the authors tested beads of smaller diameters ($50\ \text{nm}$, $1\ \mu\text{m}$, $2\ \mu\text{m}$ and $3\ \mu\text{m}$) so that they would not undergo inertial focusing in the device ($a/D_h < 0.07$). As shown on Fig. 5.13a, $50\ \text{nm}$ beads migrated completely towards the inner wall while larger beads exhibited increasing D_{inner} at $Re \sim 30\text{--}50$. For all for bead sizes, there were negligible differences in their Dean migration towards outer wall at $Re \sim 60\text{--}70$. High speed imaging at the inner wall region was also performed to further understand the distinct differences in D_{inner} by visualizing the particle flow position at different planes along

the channel height. Composite brightfield images clearly indicated increasing D_{inner} with particle size ($\sim 5.2 \mu\text{m}$ for $1 \mu\text{m}$ beads; $\sim 17.4 \mu\text{m}$ for $2 \mu\text{m}$ beads; $\sim 27.8 \mu\text{m}$ for $3 \mu\text{m}$ beads), a trend that was similar at different channel heights (Fig. 5.13b).

To determine if the subtle differences in D_{inner} during Dean migration can be exploited for separating particles with closely-spaced sizes, the authors characterized binary bead mixtures ($2 \mu\text{m}$ and $3 \mu\text{m}$ beads; $1 \mu\text{m}$ and $2 \mu\text{m}$ beads) separation performance using HiDFF at different sample to sheath flow ratios. Smaller particles (with smaller D_{inner}) were positioned closer to inner wall and separated into the inner outlet (outlet 1), while larger particles were sorted into outer outlet (outlet 2). Separation efficiency improved significantly from 20% to 60% for $2 \mu\text{m}$ bead isolation ($2 \mu\text{m}$ and $3 \mu\text{m}$ bead mixture), and from 5% to 40% for $1 \mu\text{m}$ bead isolation ($1 \mu\text{m}$ and $2 \mu\text{m}$ bead mixture) at higher sheath flow, which translated to an enrichment of the smaller particles by ~ 1000 and ~ 100 -fold, respectively (Fig. 5.14a, b). This was likely due to the smaller variation in particle initial y-position (along channel width) which enabled them to migrate laterally as a tight band towards the inner wall. As proof-of-concept for particle-based drug delivery applications, polydisperse poly(lactic-co-glycolic acid) (PLGA) microparticles were fabricated and fractionated into 3 different size groups (large, medium and small) in a 2-step HiDFF separation. Particle size and morphology were characterized using scanning electron microscope (SEM), which confirmed the distinct size differences in each group (unsorted, $3.3 \pm 0.08 \mu\text{m}$; large, $6.8 \pm 0.13 \mu\text{m}$; medium, $1.7 \pm 0.03 \mu\text{m}$; small, $0.89 \pm 0.03 \mu\text{m}$) (Fig. 5.14c).

5.3.5 Summary

So far, we have described four major types of spiral devices used for high throughput size-based particle separation. Each of these technologies has unique separation features in terms of particle size range, throughput and sample working concentration. These factors should be carefully considered when designing spiral devices for specific cells/particles sorting applications. Table 5.3 below provides a summary and comparison of key features in different spiral types.

5.4 Cell Applications

5.4.1 Cancer Cells

Cancer is the leading cause of death globally, and cancer metastasis (spreading from the primary tumor to secondary sites) is responsible for $\sim 90\%$ of cancer-related

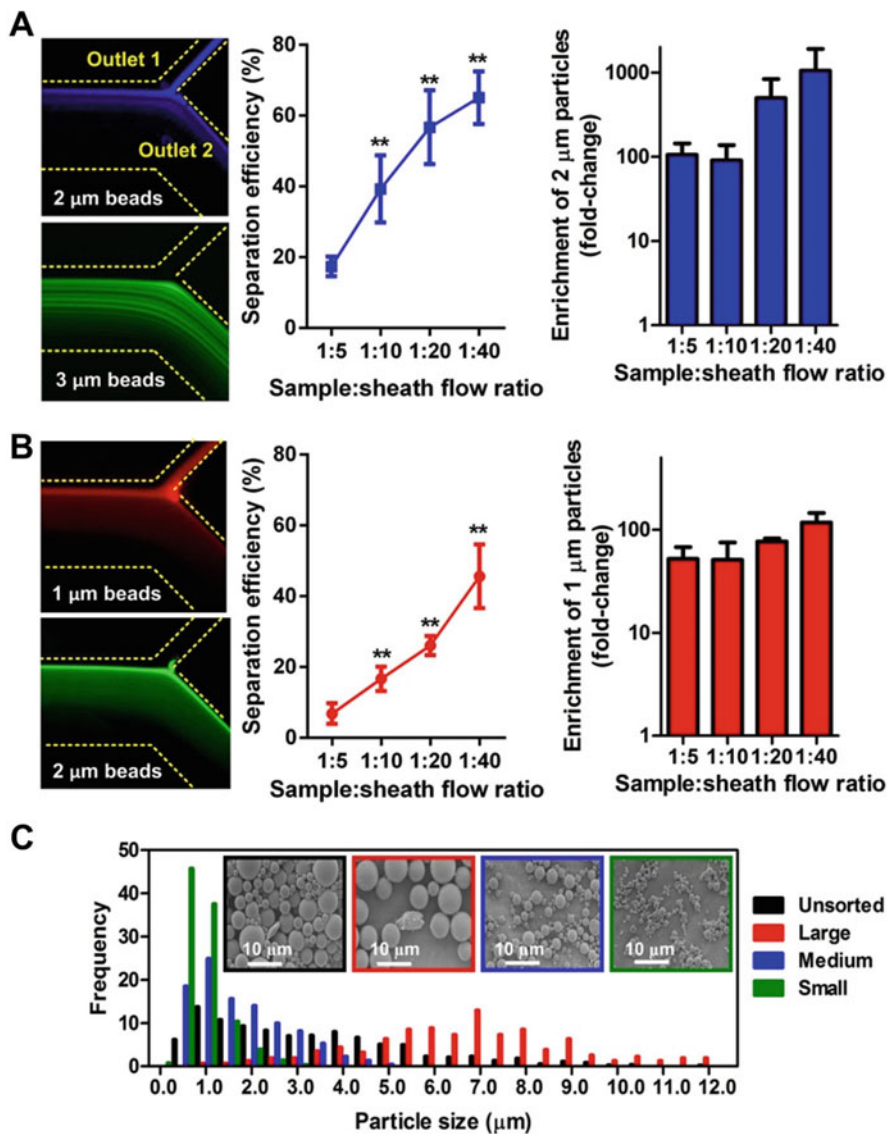



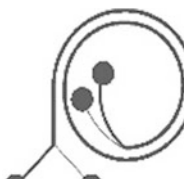
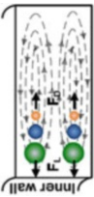


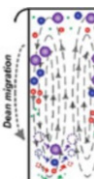



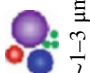


Fig. 5.14 Tunable size fractionation of microparticles using HiDFF. Average fluorescent composite images and separation performance of smaller particles at different sample to sheath flow ratio for (a) 2 and 3 μm , and (b) 1 and 2 μm binary bead mixture. *Yellow dotted lines* indicate positions of channel outlet bifurcation, (c) Size distribution plot of drug-loaded poly(lactic-co-glycolic acid) (PLGA) microparticles after a 2-step HiDFF separation into 3 sizes (large ($>5 \mu\text{m}$), medium (2–5 μm) and small ($<2 \mu\text{m}$)). Inset SEM images highlight distinct size differences between sample (inlet) and different size groups. (Reproduced with permission from Ref. [76])

Table 5.3 Comparison of different spiral devices

Type				
Principle	Rectangular spiral microfluidics 	Trapezoid spiral microfluidics 	Dean flow fractionation (DFF) 	High resolution DFF (HiDFF) 
Size	 $\sim 5\text{--}50\ \mu\text{m}$	 $\sim 5\text{--}30\ \mu\text{m}$	 $\sim 1\text{--}30\ \mu\text{m}$	 $\sim 1\text{--}3\ \mu\text{m}$
Mode	Multiplexed sorting	Binary sorting	Multiplexed sorting	Binary sorting
Flow rate	$\sim 0.5\text{--}3\ \text{mL}/\text{min}$	$\sim 0.5\text{--}6\ \text{mL}/\text{min}$	$\sim 0.1\text{--}0.2\ \text{mL}/\text{min}$ (sample flow)	$\sim 0.5\text{--}0.2\ \text{mL}/\text{min}$ (sample flow)
[Cell]	$\sim 10^{5\text{--}6}/\text{mL}$ (hematocrit)	$\sim 10^{6\text{--}7}/\text{mL}$ (hematocrit)	$\sim 10^{6\text{--}8}/\text{mL}$ (hematocrit)	$\sim 10^{6\text{--}8}/\text{mL}$ ($\sim 10\text{--}20\%$ hematocrit)
Applications	Cell separation Particle concentrator Cell alignment and ordering	Rare cell isolation Microfiltration Plasma separation	Rare cell isolation Bacterial sorting Protein purification Buffer exchange	Microvesicle isolation Nanoparticles separation Bacterial sorting

fatalities [79]. During metastasis, cancer cells are shed from primary tumors into the peripheral blood and are known as circulating tumor cells (CTCs). Recent clinical studies have shown that CTCs frequency and their genetic information can be used as surrogate biomarkers to provide critical information for cancer diagnostic and monitoring [80, 81]. However, the technical challenge for CTCs isolation lies in the rarity of these cells (~ 1 to 10 CTCs/mL) in peripheral blood (~ 5 billion RBCs/mL) [82–85]. CELLSEARCH® is the only FDA approved CTC separation technology that uses antibodies to bind to epithelial cell adhesion molecule (EpCAM) on CTCs surfaces, but EpCAM expression is highly heterogeneous which can lead to considerable capture loss.

Microfluidic CTCs separation was first reported by Nagrath et al., where they captured CTCs from patient blood using anti-EpCAM antibody functionalized microposts (CTC-chip) [86]. Following this, the same group developed a herringbone device to increase the collision and capture frequency between CTCs and antibody-coated surfaces [87]. However, the same issue related to cell surface marker heterogeneity persists in microfluidic affinity-based cell sorting. Size-based separation is hence preferred as it can significantly reduce cell loss and preserve cell viability with its label-free sorting process. In most cancer types, the size of CTCs (~ 10 – 20 μm) is larger than blood cells (WBCs ~ 8 – 12 μm ; RBCs ~ 8 μm ; platelets ~ 2 – 3 μm), and this physical difference can be exploited in spiral inertial microfluidics for high throughput cell separation.

To date, many spiral microfluidic devices have been developed for cancer cells separation (Table 5.4) [23, 51, 60, 66, 70, 88–96]. Using Dean-coupled inertial migration, Kuntaegowdanahalli et al. first reported the use of spiral microfluidics for size-dependent cancer cell sorting (Fig. 5.15a) [23]. As proof-of-concept, they separated a mixture of neuroblastoma (~ 15 μm) and glioma cells (~ 8 μm), and achieved $>80\%$ separation efficiency at a high throughput of \sim one million cells/min. These results were comparable to the performances obtained using commercial flow cytometry. To further improve the throughput, Warkiani et al. developed a multiplexed spiral device (three devices stacked together) to isolate spiked cancer cell lines from lysed blood samples. This high-throughput system can process 7.5 mL of lysed blood sample in 12.5 min and downstream fluorescence *in situ* hybridization (FISH) analysis was successfully performed on the eluted CTCs off-chip [94].

Recently, Guan et al. reported a slanted spiral device with trapezoid cross-section (80 and 130 μm in the inner and outer channel height, respectively) for cancer cell separation [64–66]. Due to the asymmetry of the channel cross-section, strong Dean vortices were generated at the outer half (deeper side) of the channel, which shifted smaller particles closer to the outer wall without affecting focusing of larger particles at the inner wall (Fig. 5.15b). They successfully isolated three cancer cell lines, MCF-7 (20 – 24 μm), T24 (16 – 17 μm) and MDA-MB-231 (10 – 15 μm) from whole blood with high recovery rate ($>80\%$) and purity (400 – 600 WBCs/mL; ~ 4 log depletion of WBCs) [66]. In another study, Aya-Bonilla et al. designed a slanted spiral microfluidic device to isolate melanoma CTCs from lysed blood sample and obtained 80% recovery rate after one round of enrichment [98]. Kulasinghe et al.

Table 5.4 Applications of spiral inertial microfluidics for cancer cell separation

No.	Sample	Spiral type	Separation performance	References
1	SH-SY5Y and neuroblastoma cells	Rectangular spiral, single inlet	Throughput: ~2 mL/min	[97]
2	Neuroblastoma and glioma cells	Rectangular spiral, single inlet	Throughput: ~10 ⁶ cells/min 90% recovery	[23]
3	MCF-7, MDA-MB-231, HeLa in 3 × diluted whole blood (15% hct)	DFF	Throughput: 100 μL/min >85% recovery	[70]
4	MCF-7, T24 and MDA-MB-231	Trapezoidal spiral	Throughput: 1.7 mL/min ≥80% recovery	[66]
5	1205Lu, A2058, SKMEL5, UACC62; Melanoma clinical samples	Trapezoidal spiral	Throughput: 1.7 mL/min >55% recovery	[98]
6	CAL27, RPMI2650, UD-SCC9, MDA-MB-486; HNC clinical samples	Trapezoidal spiral	Throughput: 1.7 mL/min 60–76% recovery	[95]
7	MCF-7 in 100 × diluted blood	Rectangular spiral, single inlet	Throughput: 400 μL/min 75.40% recovery	[93]
8	MCF-7 and HeLa	Rectangular double spiral, single inlet	Throughput: 3.33 × 10 ⁷ cells/min, 88.5% recovery	[60]
9	HeLa in 20 × diluted blood	Rectangular double spiral, single inlet	Throughput: 2.5 × 10 ⁸ cells/min ~80% recovery	[88]
10	A549 (lung adenocarcinoma)	Rectangular double spiral, single inlet	Throughput: 25 mL/h. 74.4% recovery	[92]
11	DU-145 (prostrate)	Rectangular spiral, single inlet	Throughput: ~1 mL/min 67% recovery	[96]
12	Breast and lung cancer clinical sample (lysed blood)	Multiplexed DFF	Throughput: >1.5 mL/min	[90]
13	Breast and lung cancer clinical sample (lysed blood)	Multiplexed DFF	Throughput: >0.75 mL/min 20–135 CTCs/mL recovery	[91]
14	MCF-7 in leukocytes suspension	Rectangular spiral, single inlet	Throughput: 550 μL/min >86.8% recovery	[51]
15	MCF-7 (breast)	Rectangular spiral, single inlet	Throughput: >1 mL/min ~100% recovery	[89]

also performed CTCs isolation using trapezoidal spiral microfluidics in head and neck cancer (HNC) patients, and reported the presence of CTC clusters (large group with more than five CTCs) in a subset of these cancer patients [95].

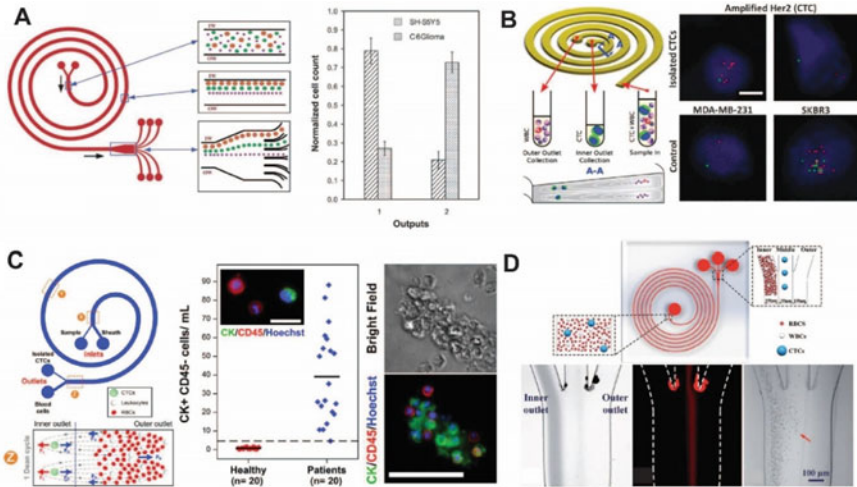


Fig. 5.15 Isolation of circulating tumour cells (CTCs) from whole blood using spiral inertial microfluidics (a) Distinct focusing and separation of microparticles ($\sim 15\text{--}20\ \mu\text{m}$, similar size range to cancer cells) into different outlets due to size-dependent inertial lift (F_L) and Dean drag (F_D) forces. Experimental results indicating efficient separation of SY5Y neuroblastoma cells from smaller C6 glioma cells. (Reproduced from Ref. [23] – published by The Royal Society of Chemistry) (b) Schematic illustration of CTCs isolation from blood using trapezoid spiral microchannels FISH analysis of HER2 expression in recovered CTCs after microfluidics isolation. (Reproduced from Ref. [66] – published by The Royal Society of Chemistry, under Creative Commons) (c) Schematic illustration of Dean Flow Fractionation (DFF) for CTCs isolation. Clinical validation of DFF in lung cancer patients. Fluorescence images and enumeration of isolated CTCs. Isolation of CTCs clusters using DFF. (Reproduced with permission from Ref. [70]) (d) Schematic illustration of a 1-inlet, 3-outlet spiral microfluidic device for cancer cell sorting. Due to the dominant F_D with smaller radius of curvature, cancer cells (MCF-7) focused inertially at the channel centre, while smaller RBCs equilibrated near the channel inner wall. (Reproduced from Ref. [93] – published by The Royal Society of Chemistry, under Creative Commons)

To increase blood processing throughput, Hou et al. developed a novel 2-inlet, 2-outlet spiral biochip for CTCs isolation based on DFF. Unlike other inertial focusing devices, the DFF device inertially focused the larger CTCs while the smaller hematologic cells (RBCs and leukocytes) were solely affected by Dean drag forces (Fig. 5.15c) [70]. This enabled accommodation of high RBCs content in the channel, which translated to a significant enhancement of RBCs processing ($\sim 20\%$ sample hematocrit) and efficient cancer cell recovery of $>85\%$.

Huang et al. also reported a simple 1-inlet, 3-outlet, 5-loop spiral cell sorter for CTCs isolation (Fig. 5.15d) [93]. Due to the smaller radius of curvature and dominant F_D , the larger cancer cells were recovered from the middle outlet, and the smaller blood cells were sorted into the inner outlet. To test the efficacy of the device, breast cancer cells (MCF-7) were spiked into diluted whole blood sample (1:100) and the device was able to remove $\sim 99\%$ of the hematologic cells after 2 rounds of separation at a throughput of $400\ \mu\text{L}/\text{min}$. The authors also reported that the processing capability can be further increased by using lysed blood samples.

Table 5.5 Applications of spiral inertial microfluidics for stem cell separation

No.	Samples	Spiral type	Separation performance	References
1	Human mesenchymal stem cells (hMSCs)	Rectangular spiral, single inlet	Throughput: 3 mL/min (~15 × 10 ⁶ cells/h)	[104]
2	Neural stem cells (NSCs)	Rectangular spiral, single inlet	Throughput: 1 mL/min >80% recovery	[106]
3	Neural stem cells (NSCs)	DFP	Throughput: 3 mL/min ~93% recovery	[107]

5.4.2 Stem Cells

Stem cells are pluripotent cells that can be induced into other cell types using physical and biochemical cues. The capabilities of self-renewal and differentiation into other specialized cells have made stem cells highly important in regenerative medicine. Unsurprisingly, an unmet need for stem cell sorting is to identify novel biomarkers to isolate subpopulations that are more pluripotent (“more stemness”). Most of the existing techniques are based on cell surface expression and labeling, but this strategy is rather challenging due to the lack of well-established surface markers and cell heterogeneity.

Recently, the biophysical properties of stem cells such as cell size, stiffness and electrical properties have emerged as potential biomarkers for stem cell sorting [99–101] (Table 5.5). One of the key physical parameters is cell size, whereby the inherent size differences can be exploited for cell cycle synchronization [102]. This physical-based method has direct advantages over common chemical-based synchronization which can affect and possibly disrupt cell physiology and metabolism [103]. Lee et al. first proposed a spiral cell sorter for high-throughput cell cycle synchronization based on cell size differences (Fig. 5.16a) [104]. To satisfy the inertial focusing criteria ($a/h > 0.07$), the channel height was set between 130 to 150 μm depending on cell types. As proof-of-concept, they demonstrated the fractionation of human bone marrow-derived mesenchymal stem cells (hMSCs) into enriched subpopulations of G0/G1, S and G2/M phases. From outlet 1, 70.4% of the cell population collected were in S and G2/M phases (~24 μm) while 86.2% of the cells in outlet 4 were from G0/G1 phase (~15 μm). The device throughput (~15 × 10⁶ cells/h) and cell viability (~95%) were much higher than those obtained by conventional methods. In a follow-up study, the group successfully identified a set of unique biophysical markers (small cell diameter, low cell stiffness and high nuclear membrane fluctuations) for the isolation of multipotent stem cells (Fig. 5.16a) [105].

Study of neural stem cells (NSCs) is pivotal for understanding disease progression and developing novel therapeutics for neurological diseases including Alzheimer’s and Parkinson’s diseases [108]. Neurospheres, which are clusters of hundreds to thousands of NSCs, are commonly used for *in vitro* study of neural precursor cells [109, 110]. To induce stem cell differentiation or conduct clonal analysis in this culture system, the original neurospheres are chemically and

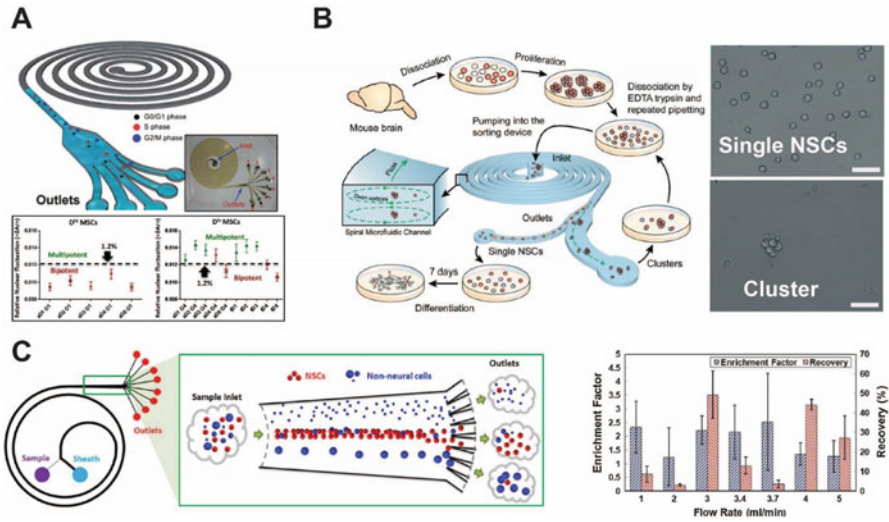


Fig. 5.16 Stem cell fractionation using spiral inertial microfluidics **(a)** Design of the 9-loop spiral microchannel for cell cycle synchronization (Adapted from Ref. [104] with permission from The Royal Society of Chemistry). Size-based sorting of mesenchymal stromal cells (MSCs) into different subpopulations for characterization of nuclear fluctuations (*NF*). (Reproduced with permission from Ref. [105]) **(b)** Overview of neural stem cells (NSCs) separation process from mice brain using spiral microfluidic device. Representative images of single NSCs and NSC clusters after separation at 1 mL/min (scale bar: 50 μ m). (Reproduced from Ref. [106] with permission from The Royal Society of Chemistry) **(c)** Schematic illustration of iPSC-derived NSCs enrichment using a 2-loop spiral cell sorter. NSCs were collected in the middle outlets, while non-NSCs (*wide size range*) were collected in all outlets. Enrichment factor and recovery of NSCs at different flow rates. (Reproduced with permission from Ref. [107])

mechanically dissociated to produce single-cell suspension and plated under stringent conditions for growth. However, the dissociated single cells are often contaminated by a small population of stem cell clusters, which can affect subsequent cell identification and clonal analysis. An effective and rapid separation method is therefore highly desirable to separate these single cells from cell clusters. As neural stem cells ($\sim 8\text{--}14\ \mu\text{m}$) are smaller than cell clusters ($\sim 40\text{--}60\ \mu\text{m}$), Nathamgari et al. developed a 1-inlet, 2-outlet spiral microdevice for size-based isolation of single cells from chemically dissociated neurospheres (Fig. 5.16b) [106]. They showed that at low flow rates (e.g. 1 mL/min), large particles (e.g. 38 μm beads or cell clusters) were focused at the center of the channel while small particles (e.g. 7.7 μm beads or single cells) were focused near the inner wall. When the flow rate was increased to 3 mL/min, the beads focusing behavior were reversed. They eventually used a flow rate of 1 mL/min and reported that $\sim 84\%$ of single cells were isolated into outlet 1 and 2 (innermost outlets), while cell clusters equilibrated in the channel centre (sorted into outlet 3–5). In addition, as neural stem cells are sensitive to shear stress, a low working flow rate can help preserve the multipotency of the stem cells with high cell viability rate ($>90\%$).

With the emergence of induced pluripotent stem cells (iPSC) technology, label-free cell purification methods are highly important for iPSC-derived cells enrichment. Song et al. designed a 2-inlet, 8-outlet DFF spiral device to enrich iPSC-derived NSCs from a heterogeneous cell mixture based on cell size differences [107]. They mixed NSCs (10–12 μm) and heterogeneously-sized non-neural cells (6–19 μm) in a ratio of 1:1 (final concentration of 2×10^6 cells/mL), and processed the sample at a flow rate of 3 mL/min. As expected, the NSCs focused into a tight band and were sorted into the middle outlets (outlet 4 and 5), while the non-neural cells were remained randomly distributed across the channel width and the larger cells were sorted into the inner wall outlets (outlet 7 and 8). They reported ~ 2.1 fold NSCs enrichment with a 93% recovery rate (Fig. 5.16c). A major limitation lies in the low purity, as the device is unable to deplete non-neural cells of similar sizes as NSCs.

5.4.3 Immune Cells

Neutrophils are the most abundant leukocytes in human blood and the key effector cells of the innate immunity. They are also implicated in major diseases including type 2 diabetes mellitus (T2DM) [111], cancer [112] and cardiovascular diseases [113]. In TD2M, numerous neutrophil dysfunctions such as cell stiffening [114, 115], impaired chemotaxis [116, 117] and phagocytosis [118] can lead to an increased susceptibility to bacterial infections. Traditionally, neutrophils are isolated using laborious methods such as density gradient centrifugation and RBC lysis, which not only require a large blood sample volume (>10 mL), but are also prone to induce neutrophil activation if not properly done. Commercial neutrophil isolation kits that utilize immunomagnetic labeling have been developed to negatively select untouched neutrophils (MACS xpress® (Miltenyi Biotec) and Easy Sep™ (STEMCELL Technologies)), but these kits are expensive and not practical for large volume processing. Developing an efficient and cost-effective neutrophil sorting strategy is therefore necessary for accurate phenotyping in neutrophil studies and point-of-care testing. Table 5.6 shows a summary of spiral microdevices developed for this purpose.

Table 5.6 Applications of spiral inertial microfluidics for immune cell separation

No.	Samples	Spiral type	Separation performance	References
1	Monocytes in $10 \times$ diluted blood	Rectangular spiral, single inlet	Throughput: 1.1 mL/min Recovery: not reported	[96]
2	Neutrophils in lysed blood	DFF	Throughput: 130 $\mu\text{L}/\text{min}$ $>90\%$ purity	[119]
3	Leukocytes in $200 \times$ diluted blood	Trapezoidal spiral	Throughput: 0.8 mL/min $>80\%$ recovery	[65]
4	Leukocytes in $500 \times$ diluted blood	Rectangular spiral, single inlet	Throughput: 1.8 mL/min $\sim 95\%$ recovery	[120]

Capitalizing on the high separation resolution of DFF, Hou et al. developed a 4-outlet DFF device to purify neutrophils from whole blood without antibodies labelling. The separation is based on subtle cell size differences among leukocyte subtypes (neutrophils/monocytes (10–12 μm); lymphocytes (7–8 μm)) (Fig. 5.17a) [119]. This device only required small amount of blood (finger prick; $\sim 100 \mu\text{L}$) for neutrophil isolation, and sorted neutrophils also undergo simultaneous washing as they were eluted in fresh saline solution due to the buffer exchange capabilities of DFF. The group further characterized the rolling behavior of sorted neutrophils on E-selectin using microfluidics. In their clinical validation using healthy subjects and patients with T2DM, this developed microfluidic-based neutrophil sorting and phenotyping strategy revealed a significant difference in neutrophil rolling pattern between both groups, clearly suggesting neutrophil rolling speed as a potential functional biomarker for inflammatory profiling in T2DM patients.

In general, conventional blood cell separation methods (centrifugation, FACS, MACS) are laborious and highly dependent on user operation, and the phenotype of isolated leukocytes could be altered if not done carefully. To address these issues, Wu et al. developed a spiral microfluidic device with a trapezoid cross-section to isolate the larger leukocytes ($\sim 8\text{--}12 \mu\text{m}$) from diluted whole blood (RBCs $\sim 6\text{--}8 \mu\text{m}$) [65]. The schematic in Fig. 5.17b illustrates the device design and working principle. At optimized working conditions, the device can separate polymorphonuclear leukocytes (PMNs) and mononuclear leukocytes (MNLs) from diluted human blood (1–2% hematocrit) with high efficiency ($>80\%$). In addition, the activation in the device-sorted PMNs was negligible as compared to lysis method. Nivedita et al. also developed an Archimedean spiral device with $<8 \text{ cm}$ focusing length for leukocytes separation in diluted blood sample (1:500) at a flow rate of 1.8 mL/min, and achieved a high separation efficiency ($\sim 95\%$) and throughput (up to 1×10^6 cells/min) (Fig. 5.17c) [120].

5.4.4 Sperm Cells

Assisted reproductive techniques (ART) have benefited countless couples experiencing infertility, and one major aspect of ART is to select healthy spermatozoa *in vitro* fertilization (IVF). Traditionally, sperm cells are prepared using serial centrifugation or the swim-up methods, but repeated handling and centrifugation can cause damage to the sperm cells' DNA, or lead to the production of reactive oxygen species (ROS) [121, 122]. Conventional sperm cell sorting methods using microfluidics relies on sperm motility, but the approach is unable to identify viable but non-motile sperms for intracytoplasmic sperm injection, which is relevant for patients suffering from severe or complete asthenozoospermia [122]. Taking advantage of the size difference between sperm and blood cell, Son et al. developed a spiral microfluidics sperm cell sorter for non-motile sperms separation. (Fig. 5.18a) [123]. Sperm cells (1–2 million/mL) were mixed with RBCs (7–9 million/mL) and introduced into the spiral channel. At a flow rate of 0.52 mL/min, 81.2% of the sperm cells were sorted into the

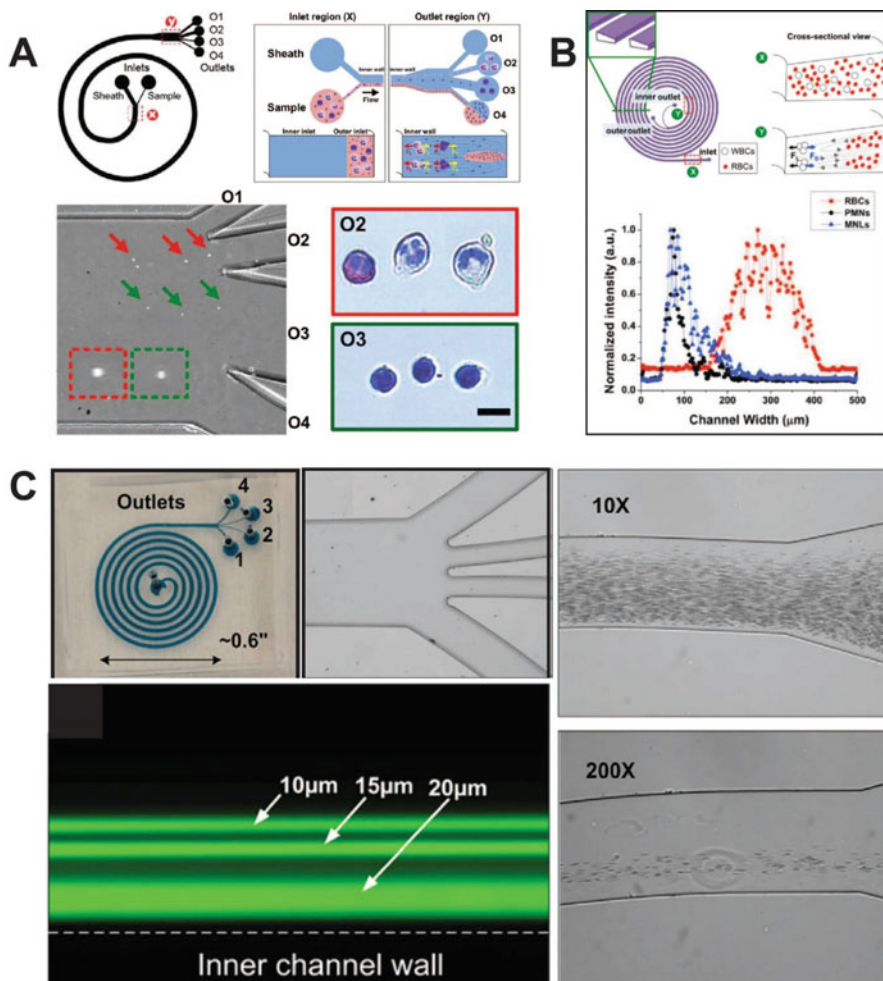


Fig. 5.17 Immune cells isolation using spiral inertial microfluidics (a) Rapid size-based neutrophil sorting and washing using DFF. High speed images indicating distinct focusing of larger neutrophils and smaller lymphocytes into different outlets. (Adapted from Ref. [119] under Creative Commons), (b) Immune cell isolation using trapezoid spiral device. Intensity line scans indicating distribution of polymorphonuclear leukocytes (PML), mononuclear leukocytes (MNL), and RBCs across channel width (Reprinted (adapted) with permission from Ref. [65]. Copyright (2014) American Chemical Society.) (c) Images of the 1-inlet, 4-outlet Archimedean spiral device ($<1 \text{ in.}^2$). Focused streams of three particle populations ($10 \mu\text{m}$, $15 \mu\text{m}$ and $20 \mu\text{m}$ in diameter) at a flow rate of 2.2 mL/min . Images of focused RBCs at the outmost loop of spiral channel with 10 and 200-fold diluted whole blood. (Reproduced with permission from Ref. [120])

outer two outlets, while 99% RBCs were separated into the inner two outlets. As shown in Fig. 5.18b, the smaller sperm cells formed a broad focusing band near the channel centre, which can be attributed to their asymmetrical and irregular shape

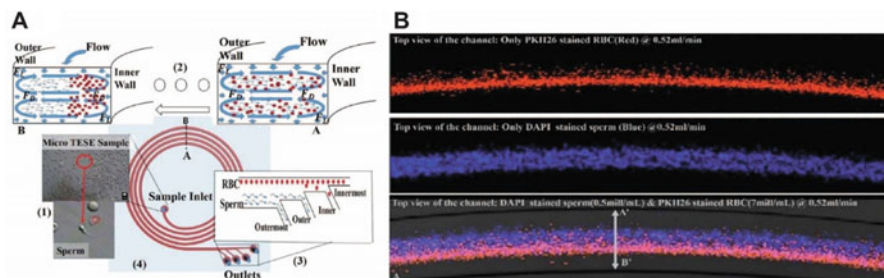


Fig. 5.18 Sperm cell isolation using spiral inertial microfluidics (a) Separation principle of sperm cells from RBCs using spiral microchannels (b) Fluorescent images of the focusing positions of sperm cells (blue) and RBCs (red) at a flow rate of 0.52 mL/min. (Adapted with permission from Ref. [123])

Table 5.7 Applications of spiral inertial microfluidics for microbes and biomolecules separation

No.	Samples/application	Spiral type	Separation performance	References
1	Non-motile sperm cell	Rectangular spiral, single inlet	Throughput: 0.52 mL/min 81% recovery	[123]
2	<i>E.coli</i> , <i>K. pneumoniae</i> , <i>P. aeruginosa</i> , <i>S. aureus</i> , <i>E. faecalis</i>	DFF	Throughput: 1.7 mL/min ~75% recovery	[73]
3	Algal cells	Rectangular spiral, single inlet	Throughput: 3.2 mL/min 77% recovery	[125]
4	<i>Phytophthora ramorum</i> sporangia	Rectangular spiral, single inlet	Throughput: 2 mL /min 95% recovery	[126]
5	Antibodies in serum	DFF	Throughput: 130 μ L /min >80% recovery	[130]
6	Aptamer	DFF	Throughput: 160 μ L /min ($\sim 2 \times 10^6$ cells/min) $\geq 10^6$ partitioning efficiency	[74]

(length of $4.79 \pm 0.26 \mu\text{m}$ and width of $2.82 \pm 0.23 \mu\text{m}$). In contrast, larger RBCs ($\sim 7.5\text{--}8.7 \mu\text{m}$) inertially focused into a tight stream at the inner wall, thus achieving separation (Table 5.6).

5.4.5 Microbes

Microorganism separation using spiral microfluidics (Table 5.7) is an area of considerable interest for bacterial diagnostics and environmental monitoring [124]. A major difference between microorganism and cell isolation is that microbes are smaller ($\sim 1\text{--}3 \mu\text{m}$) as compared to mammalian cells ($\sim 10\text{--}20 \mu\text{m}$), and thus will

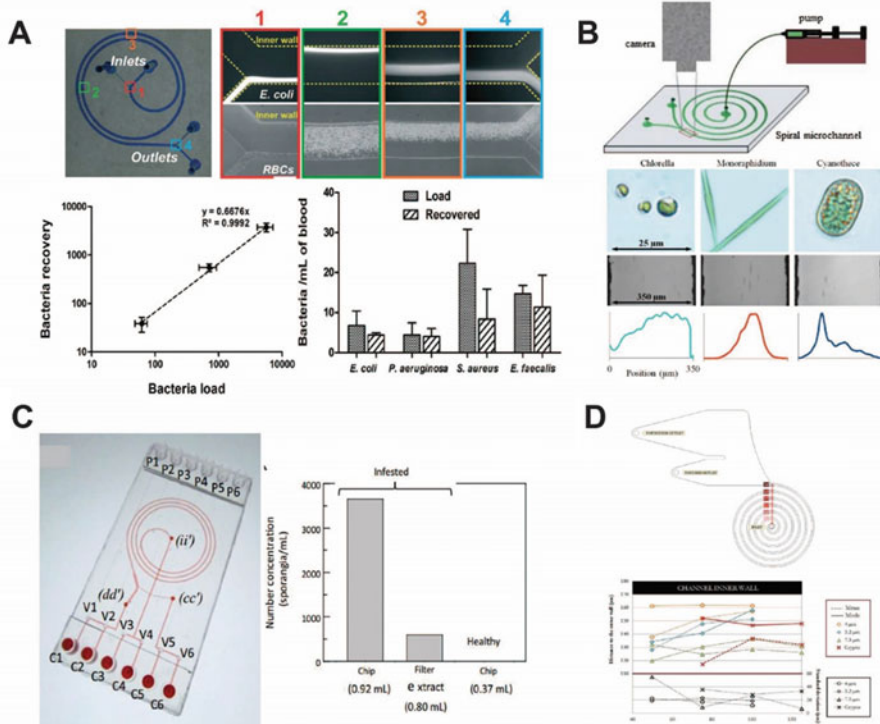


Fig. 5.19 Microbe isolation using spiral inertial microfluidics (a) Bacterial isolation using DFF. Plots indicating high bacterial recovery rate (>65%) at different bacterial loads and for low abundance bacteria (~10–50 CFU/mL). (Reproduced from Ref. [73] – published by The Royal Society of Chemistry.) (b) Experimental setup for bacteria separation using spiral microchannel. Images of different algae species (*Chlorella*, *Monoraphidium* and *Cyanobacterium*) and their focusing position across the channel width at 1.6 mL/min. (Reproduced from Ref. [125] under Creative Commons) (c) Photograph of a multi-layered microdevice consisting of pneumatic microvalves, spiral microchannel and fluid control channels. Significant enrichment of *P. ramorum* sporangia from infested *Rhododendron* leaves using the developed spiral sorter (Adapted with permission from Ref. [126]) (d) Spiral microfluidic channel for pathogens separation. Distribution of *C. parvum* as a function of distance to the outer wall. (Reproduced from Ref. [129] under Creative Commons)

experience less inertial (or drag) forces. Hence, channel dimensions have to be scaled down significantly to achieve similar inertial focusing effects.

To overcome this issue, Hou et al. utilized the DFF technique to isolate low abundance bacteria from whole blood based on cell size difference (Fig. 5.19a) [73]. By using a sheath flow to “pinch” the bacteria-containing blood sample at the inlet, they demonstrated well-controlled Dean migration of bacteria towards the outer wall while larger blood cells remained inertially focused near the inner wall to achieve separation. This approach enables continuous, species-independent

isolation of clinical bacteria isolates spiked at low concentrations ($\sim 10\text{--}50$ CFU/mL) from whole blood without affinity-based target labelling.

Besides bacteria, algae are also widely studied as they are often used as bio-sensors for monitoring and detecting environmental changes. Traditional manual algae identification method includes microscopy-based manual identification which is time-consuming and limits the sampling resolution. To automate the identification process, Schaap et al. developed a spiral inertial microfluidic device for algal cells separation based on cell size and shape [125]. Three morphologically different species of algae were used in the experiment: (i) *Chlorella* (spherical shaped, diameter of 6.0 ± 1.0 μm); (ii) *Cyanothece* (prolate spheroid shape, 15.6 ± 2.3 μm in long axis and 11.1 ± 1.0 μm in short axis); and (iii) *Monoraphidium* (cylindrical shape, 54.6 ± 14 μm in length, diameter of 3.14 ± 0.6 μm). The authors found that the shape of the algae can affect inertial focusing behavior in spiral channels. Even though *Cyanothece* and *Monoraphidium* possess equivalent spherical diameter, they can be separated based on their geometrical difference and a separation efficiency of 77% was achieved at a flow rate of 3.2 mL/min. The prolate spherical *Cyanothece* behaved similar to a 10 μm particle, while *Monoraphidium* has an effective diameter of 3.14 μm in the plane perpendicular to the flow, and thus experienced less lift forces as compared to *Cyanothece*. Since *Chlorella* did not fulfil the inertial focusing criteria, they remained randomly distributed spread across the channel. The experimental setup, algae images and distribution across the channel cross section are shown in Fig. 5.19b.

Phytophthora ramorum is a fungal plant pathogen that infects a large number of plant species and results in extensive damage to ecosystem. Hence, it is imperative to detect and prevent the spread of this fungus. The *P. ramorum* generally presents an ovoid shape with diameter ranging from 20 to 40 μm . To achieve efficient inertial focusing effects, Clime et al. developed a spiral microfluidic platform with a channel depth of 200 μm and width of 600 μm . The device was integrated with peristaltic microvalves for fluid operation and process control. Using samples derived from infested plant leaves, they were able to obtain 6.1-fold concentration of the fungi (Fig. 5.19c) [126].

Another crucial environmental application is the detection of waterborne pathogens in drinking water. It is a challenging task as pathogens are usually present in low numbers. For example, the presence of *Cryptosporidium* oocysts was reported less than 10 per 10 liters in the recreational lakes in Amsterdam, The Netherlands [127]. The standard waterborne pathogen monitoring process involves complex procedures including filtration, immune-magnetic separation, fluorescence staining and microscopy-based examination. These methods require long processing time (several days), expensive equipment and highly trained expertise [128]. In a work by Jimenez et al., they presented a 6-loop spiral focusing microchannel with depth of 30 μm and width of 170 μm to separate waterborne pathogens (Fig. 5.19d) [129]. The device has two wide outlets to enhance particle positions discrimination and separation resolution. To demonstrate the feasibility of this device, they separated waterborne pathogen *Cryptosporidium parvum*, ($\sim 4\text{--}5$ μm) at a high flow rate of 500 $\mu\text{L}/\text{min}$ with a separation efficiency of 100%.

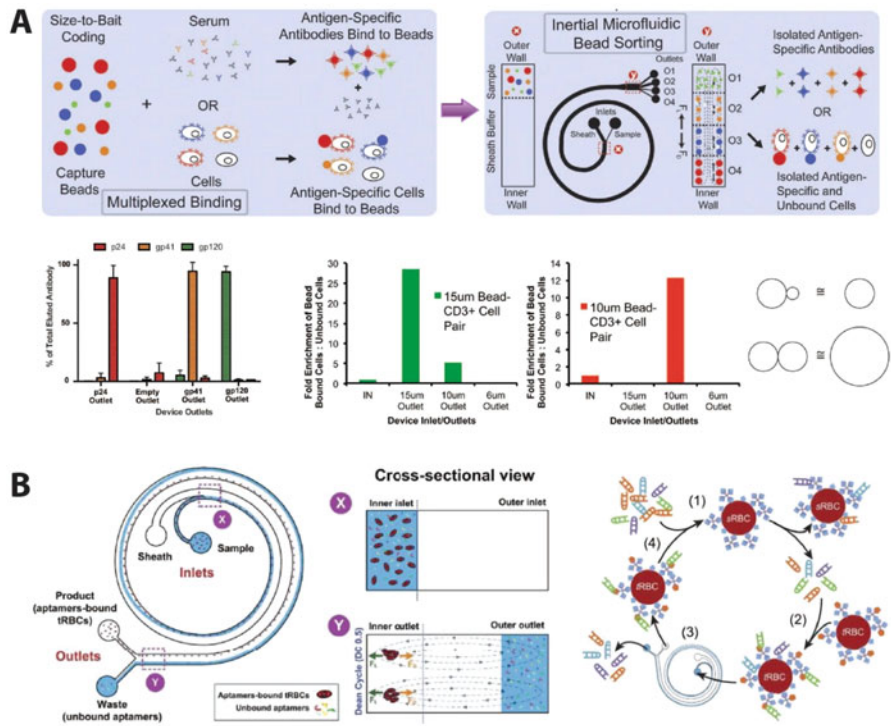


Fig. 5.20 Biomolecule separation using spiral inertial microfluidics (a) Workflow of multiplexed proteins or cells sorting using DFF coupled with affinity-based bead binding. Results indicating efficient separation of 3 major HIV antigen-specific antibodies, as well as the enrichment of bead-bound CD3+ lymphocytes. (Reproduced from Ref. [130] under Creative Commons) (b) Schematic illustration of the inertial microfluidic SELEX (iSELEX) for aptamer selection. Cells with bound aptamers are focused along the inner wall while the unbound aptamers migrate completely to the outer wall. (Adapted from Ref. [74] under Creative Commons)

5.4.6 Biomolecules

Purification of proteins or other biomolecules from complex background is essential in many biomedical applications and molecular assays. Unlike mammalian cells or bacteria, biomolecules are significantly smaller (nanometer scale) and hence challenging to establish inertial focusing effects. A possible strategy is to bind target biomolecules to functionalized microparticles to “artificially enhance” their sizes (Table 5.6). This unique method is presented in a work by Sarkar et al., where they reported a multiplexed affinity-based protein separation platform using DFF [130]. The working principle is shown in Fig. 5.20a. As proof-of-concept for HIV diagnostics, HIV antigens p24, gp41 and gp120, were coated on beads of three different sizes (10 μm, 4.5 μm and 1 μm) respectively to serve as capture agents. The coated beads were then incubated with serum obtained from HIV-infected patients

and introduced into the DFF device. Based on inertial focusing effects, beads were sorted into different outlets based on their size. The captured antibodies were then eluted from the beads for analysis. Compared to traditional antibody purification methods, this high throughput sample processing platform (10^4 – 10^7 beads/s, milligram-of proteins) provided a ~ten-fold time reduction while enabling multiplexed protein purification.

Aptamers are short nucleic acid or peptide molecules that can selectively recognize distinct epitopes [131]. SELEX (systematic evolution of ligands by exponential enrichment) is a combinatorial chemistry technique used for selecting binding aptamers from a large random sequence pool *in vitro*, but this process is often iterative and time-consuming [132, 133]. To increase the selection efficacy, Birch et al. developed a novel microfluidic aptamer selection strategy based on the SELEX principle and DFF, termed as I-SELEX (Fig. 5.20b) [74]. Briefly, the pre-incubated cells and aptamer library mixtures were introduced into the spiral device. Due to distinct size differences between RBCs and nucleic acid molecules, unbound aptamers migrate along the Dean vortices towards the outer wall while the larger cells focus inertially near the inner wall. By using a wider spiral channel, the large separation distance between the unbound aptamers and aptamers-binding cells resulted in a high partition efficiency of $\sim 10^6$, which is comparable to the traditional “gold standard” capillary electrophoresis-based methods [134]. Besides high throughput processing ($\sim 2 \times 10^6$ cells/min), the developed technology was also used to identify novel high-affinity binding aptamer targets for malaria-infected RBCs.

5.5 Recent Advances

5.5.1 Novel Spiral Designs and Microstructures

Inspired by trapezoidal spiral devices, one can modulate the Dean vortices to manipulate particle focusing behavior by varying the channel geometries. For example, Sonmez et al. utilized an asymmetric serpentine channel design in a spiral device [135]. Due to the superposition of two different secondary flows induced by serpentine and spiral geometries, they demonstrated an increase in focusing quality of 9.9 μm beads as compared to conventional spiral and serpentine channels. The device can achieve $\sim 99.5\%$ purity of sorted 9.9 μm beads at flow rate of 2.5 mL/min.

In recent studies, circular channels are used in spiral devices without relying on conventional microfabrication techniques [62, 136]. This can be achieved by using Tygon® tubing [136] or circular cross section PDMS tube [62] wrapped around 3D-printed barrel to form curvilinear or helical structures (Fig. 5.21a). A key advantage of this strategy is that it is cheap and highly customizable as one can easily change barrel size and tubing diameter to modify the radius of curvature and channel dimension, respectively. Another attractive feature is that the tubings can be connected in a “plug-and-play” mode to other PDMS based microfluidic devices,

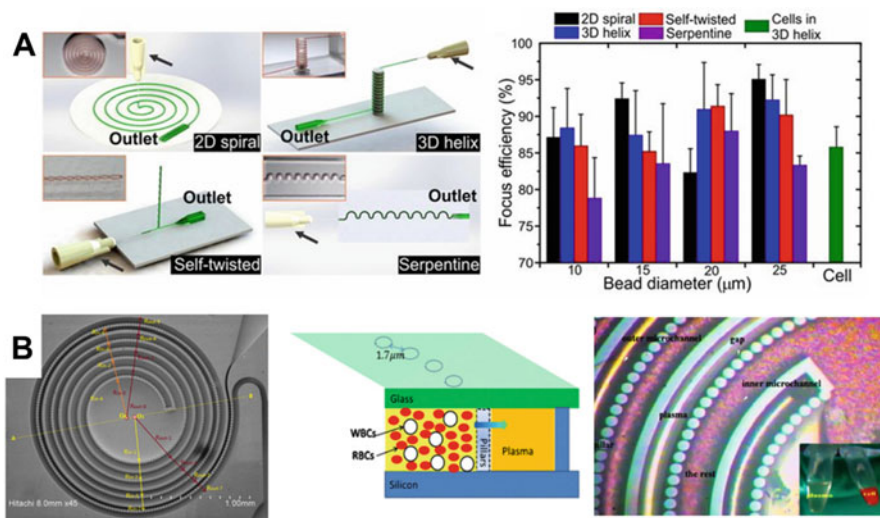


Fig. 5.21 Novel spiral designs and microstructures: (a) (left) Various designs of spiral inertial microfluidics created using circular PDMS microtubes. (right) Characterization of particle focusing efficiencies in different device designs. (Reproduced with permission from Ref. [62]) (b) (left) Spiral channel with micropillar array for plasma extraction. (center) Schematic illustration of separation principle. (right) Microscopic image showing efficient plasma extraction and RBCs retention. (Reproduced with permission from Ref. [137])

thus enabling in-line integration with different modalities. Hahn et al. utilized Tygon[®] tubing (inner diameter 190 μm, outer diameter 2 mm) in a helical spiral device and demonstrated separation of 15 and 25 μm particles into different outlets with recovery rates of $50.9 \pm 5.3\%$ and $99.5 \pm 0.9\%$, respectively [136]. Xi et al also fabricated various designs of serpentine and spiral devices using circular PDMS tube (100 μm for inner diameter), and achieved high focusing efficiencies (>75%) for particle size ranging from 10–25 μm (Fig. 5.21a) [62]. For novel designs such as helical spiral and self-twisted spiral, an interesting feature is that Dean number (De) and radius of curvature remain constant for each loop as opposed to the standard planar Archimedean spiral devices [62]. The self-twisted spiral device also exhibits a stronger Dean flow profile due to the smaller radius of curvature.

Several groups have also introduced patterned microstructures such as micropillars or confined regions in their spiral channels [137, 138]. The presence of these obstacles induces additional secondary flow which can be exploited to manipulate particle position together with Dean flow to enhance separation efficiency [34]. Geng et al. designed a micropillar array (1.7 μm gap) in spiral channel for blood plasma extraction from diluted whole blood (Fig. 5.21b) [137]. Due to the combinatorial effects of physical filtration in pillar array and lateral Dean flow effects, “cell-free” plasma effectively filters through the micropillars towards the channel outer wall while the blood cells are retained in inner wall. Another important feature is the decreasing distance between pillars and the inner wall along the

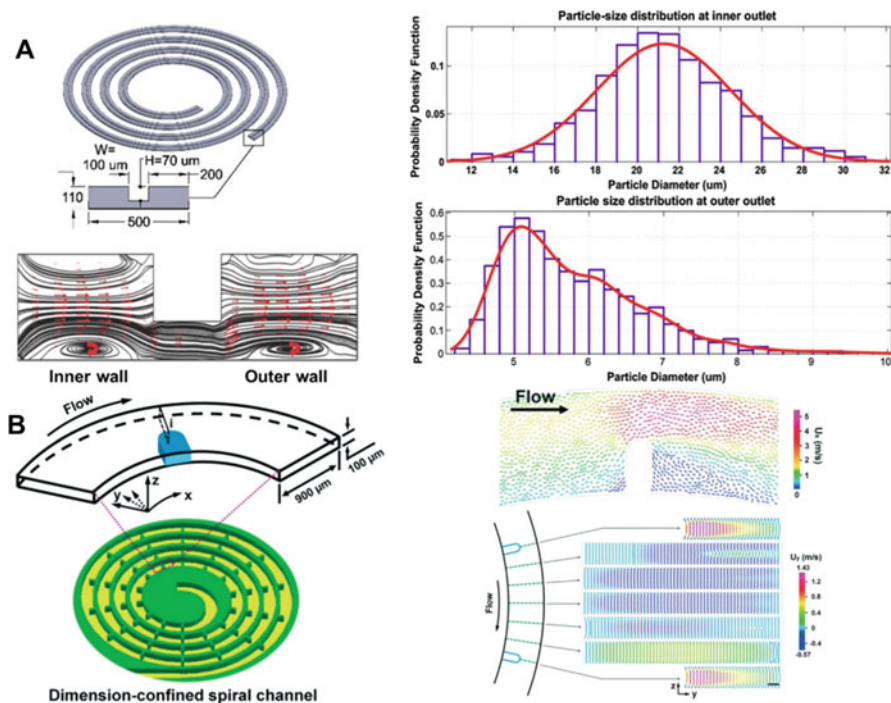


Fig. 5.22 Novel spiral designs and microstructures 2: (a) (left) Schematic illustration of the spiral device with stair-like cross-section. Cross-sectional view of the Dean vortices generated in the device. (right) Particle size distribution from the inner outlet and outlets. (Reproduced with permission from Ref. [138]) (b) (left) Spiral channel design with micro-obstacles. Velocity profiles at the confined region in xy plane (right top) and zy plane (right bottom) using fluid simulation. (Reproduced from Ref. [139] – published by The Royal Society of Chemistry)

microchannel to enhance the volume of extracted plasma. At an optimal flow rate of $10 \mu\text{L}/\text{min}$, their device achieved 49.6% separation ratio (plasma volume to initial sample volume) from $250 \mu\text{L}$ of $20\times$ diluted blood. Ghadami et al. also developed a novel spiral device with stair-like cross section in which the channel was divided into 3 sections namely inner, intermediate and outer wall [138] (Fig. 5.22a). Instead of having two counter-rotating Dean vortices in conventional spiral devices, the Dean vortices are positioned adjacent to each other with one located at the inner wall section and another at the outer wall section. Similar to DFF, larger particles would migrate towards the inner wall section while smaller particles remain in the outer wall section. They reported that the device can achieve a large separation distance of $260 \mu\text{m}$ between $7 \mu\text{m}$ particles and $20 \mu\text{m}$ particles. Recently, Shen et al. investigated various spiral designs with ordered narrow regions (Fig. 5.22b) [139]. As the fluid flows into the narrow regions, the increasing fluid velocity provides additional secondary flow acceleration which results in enhancement of particle focusing. To demonstrate the separation performance of the developed devices, they successfully sorted MCF-7 (97.5%) and HeLa (92.3%) cancer cells from diluted whole blood

(~2.5% hct) at 6.5 mL/min. Furthermore, they also performed blood plasma extraction at a lower flow rate of 3 mL/min whereby the blood cells were focusing close to the outer wall (removed through outer outlet) and plasma was extracted from other outlets. They reported a high blood cells rejection efficiency (99.96%) and plasma recovery (67.6%) from diluted blood (~2.5% hct) samples.

5.5.2 *Integrating Multiplexing Spiral Devices*

Unlike straight channel designs, a major limitation for spiral or curvilinear devices is the difficulty for massive planar parallelization to achieve higher throughput. To facilitate high volume processing, the spiral stacking strategy has been reported by several groups [67, 91, 140–143]. Khoo et al. developed a multiplexed spiral microfluidic device for label-free enrichment of CTCs at ultra-high throughput [140]. The stacked device was fabricated by stacking three spiral channels vertically with shared common inlets and outlets (Fig. 5.23a). To demonstrate the feasibility of this device, the authors processed blood samples (7.5 mL) from 10 healthy donors and 58 patients with metastatic breast or non-small cell lung cancer. The throughput was significantly enhanced (20-fold higher) which translated to processing 7.5 mL in less than 5 min with 100% detection sensitivity and high selectivity. Based on similar concept, Warkiani et al. utilized a stack of 40 trapezoidal spiral devices for CHO cell and yeast cells separation at 240 mL/min. [67]. Rafeie et al. later demonstrated multiplexing of 16 trapezoidal spiral devices on one layer for blood plasma separation from diluted blood [142]. They managed to achieve ~100% cell rejection ratio for ~0.5%–1% hematocrit at an optimal flow rate of 1.5 mL/min for a single device (24 mL/min for 16 devices). For stacking multiple devices, it should be noted that the top surface of the PDMS devices needs to be flat to prevent leakages between 2 consecutive layers. Precise alignment of the inlet and outlet ports is necessary to ensure that each device layer can receive equal flow distribution. In addition, stacking of multiple devices can suffer from slight pressure variance and might possibly affect individual device performance. To overcome these problems, several groups have introduced custom design manifold to distribute fluid flow equally. For example, Miller et al. developed a manifold to control pressure-driven flow in each spiral device [141]. As shown in Fig. 5.23b, they successfully incorporated 20 devices which can provide a large separation size range (2–300 μm) at a throughout of 1000 mL/min. Additionally, the system includes several unique sample processing features such as cascaded channels to enhance separation efficiency, and sample recirculation to increase purification and yield (Fig. 5.23c).

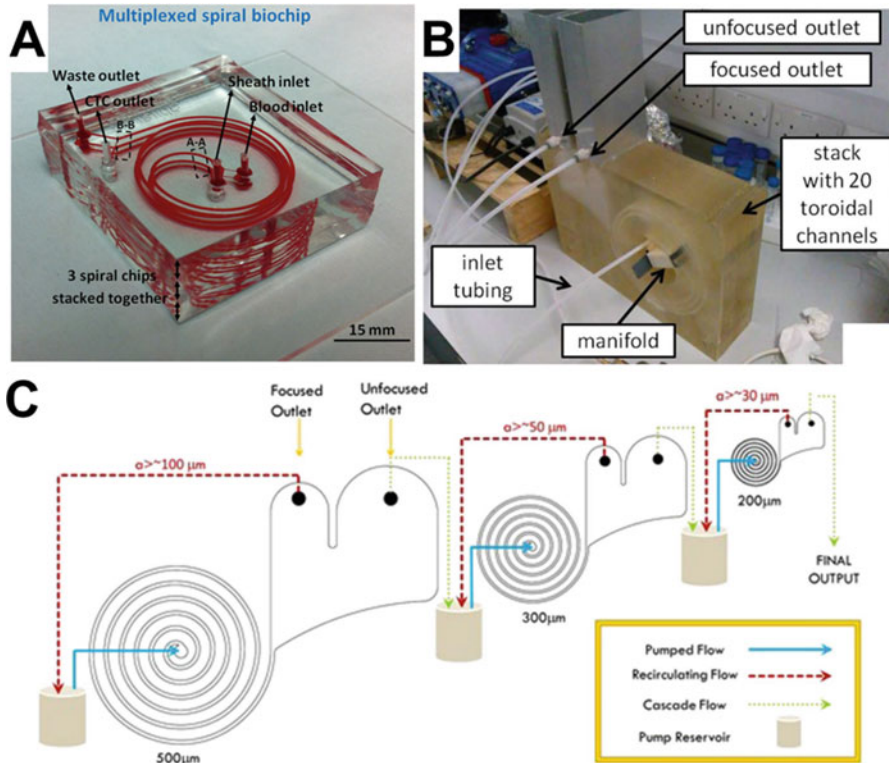


Fig. 5.23 Integrated multiplexing spiral devices: (a) Photo of a multiplexed spiral device by stacking 3 spiral devices together for high throughput CTCs isolation. (Adapted from Ref. [140] under Creative Commons) (b) Image of a stacked spiral system for large range particle separation (c) Schematic illustration of cascaded sample processing using different spiral devices. (Reproduced from Ref. [141] under Creative Commons)

5.5.3 Multiple Stage Spiral Device

Multiple stage spiral devices have been proposed to enhance sorting performance [141, 144]. Robinson et al. developed a two-stage spiral device for RBC depletion from diluted whole blood (2% hct). As a single spiral separation could not achieve high WBCs purity, they added another stage of separation at the end of first spiral device which has a bifurcation that equally splits into two smaller daughter spiral devices; one for subsequent RBCs exclusion and another one for transporting sorted RBCs to waste and balancing the fluidic resistances. They showed the device can effectively eliminate RBCs from diluted whole blood with 30-fold increase in RBCs depletion as compared to a single-stage spiral device [144].

5.5.4 Closed-Loop Sample Processing

Besides multiple stage sorting, recirculation strategy is another attractive alternative for processing of complex biofluid such as blood or high cell concentration samples [141, 143, 145]. Briefly, sample recirculation is achieved by using peristaltic pump to feed output eluent (containing target cells) back to the inlet sample reservoir so that the suspension can pass through the device again. The recirculation strategy provides several benefits. First, it continuously dilutes and removes the waste materials that can otherwise affect the separation performance. Secondly, it will enrich target cells into smaller volumes for subsequent processing without manual handling. In most cell sorting applications, the target cells in the samples are usually rare and do not contribute much to the sample concentration. Hence, the target cells recirculation will not compromise the separation performance. Fig. 5.24a shows a recirculation strategy developed by Ryu et al. [145]. In this work, they utilized spiral inertial microfluidics with recirculation strategy to extract polymorphonuclear leukocytes from patient-derived airway secretion or sputum. As sputum is highly complex and heterogeneous among patient sample, a single step sorting is often insufficient to achieve satisfactory separation performance. Recirculation can purify target cell suspending medium while continuously eliminates mucin aggregates from sample. The reported device retrieved ~95% PMNs from sputum from six patients and provided superior performance over traditional Sputalysin (DTT) protocol (Fig. 5.24a (right)). Kwon et al. recently described a closed-loop multiplexing spiral system for perfusion culture of Immunoglobulin G1 (IgG1) CHO cells with high IgG1 recovery rate (>99%), cell viability (>97%) and long term stability (18–25 days) [143].

5.5.5 Integrating with Other Separation Modalities

Coupling spiral microfluidics with other cell sorting modalities was recently proposed by Nivedita et al. [96]. In this work, they described a novel integrated platform which comprised of a spiral separator and a second-stage cell sorter based on lateral cavity acoustic transducer (LCAT). Briefly, angled lateral channel array was designed to trap air as depicted in Fig. 5.24b. Acoustic field was applied to the device which resulted in oscillation of the air/liquid interface and generation of microstreaming vortices. When larger particles approached these microvortices, they would be trapped into the circulating inner streamlines as smaller particles followed along the outer streamlines with the bulk flow [96]. By adjusting excitation voltage of acoustic actuator, the device can selectively capture different sized particles to further enrich target cells. As proof-of-concept, they applied the device to trap larger monocytes (>18 μm) from $10 \times$ diluted blood. Smaller RBCs and WBCs, and intermediate sized cells (<18 μm) were eliminated to outlet 1 (spiral outlet) and outlet 2 (LCAT), while enriched larger monocytes remained trapped inside LCAT

part. By flushing PBS through the channel, they were able to retrieve and concentrate target cells with an enrichment of 987-fold. They also demonstrated separation of DU-145 cells ($>16\ \mu\text{m}$) from highly heterogeneous DU-145 population ($7\text{--}28\ \mu\text{m}$) and achieved 91.7% purity and 67.5% recovery rate of target cells. Noteworthy, this work showed the unification of two separation techniques operating at different flow rates ($1500\ \mu\text{L}/\text{min}$ and $25\ \mu\text{L}/\text{min}$). This was achieved by adjusting the pressure drop/hydraulic resistance of the spiral outlet and transition region between 2 devices. Another simple modification that can assist in enrichment of cells was proposed by Wang et al. [92], in which they added a membrane filter at the outlet of the spiral device to further enrich CTCs for immunostaining.

For blood cell sorting applications, it remains challenging to use whole blood as a direct input for spiral devices due to the high RBCs concentration (~ 5 billion/mL) and secondary cell-cell interactions are known to have adverse effects on sorting performance [69, 146]. This makes off-chip sample pre-processing (dilution or RBC lysis) a prerequisite prior spiral separation. Recently, Ramachandraiah et al. proposed an integrated spiral device for leukocyte fractionation with on-chip RBC lysis (Fig. 5.24c) [146]. Whole blood and hypotonic solution (deionized water) were introduced into the device to selectively lyse the RBCs. The integrated lysis chamber with expansion chambers helped increase residence time for proper RBCs lysis. The lysed blood was then washed with sheath buffer stream (PBS) to prevent negative effects such as leukocytes swelling. Finally, the focused sample stream proceeded through the double spiral channel to fractionate out granulocytes, monocytes, and lymphocytes with a purity of 86%, 41% and 91% respectively. Such integrated device is favorable for point of care systems as it facilitates user operation and is less time-consuming process compared to sequential sample processing. Furthermore, it reduces cell loss that can occur during sample handling between each process. It should be noted that the abovementioned device required three syringe pumps to operate which can be a major drawback for point of care applications.

5.6 Conclusions and Future Outlook

Spiral inertial microfluidics has emerged as a superior separation technique for high throughput particle sorting in biomedical applications and clinical diagnostics. Since the introduction of inertial microfluidics by Di Carlo et al. [30] and the first demonstration of spiral microchannels for particle filtration [147] a decade ago, enormous efforts by us and other groups have focused on exploiting this technology for different cell sorting applications, achieving higher throughput by multiplexing, and enabling small micro and nanoparticles separation. Compared to other microfluidics systems, the key advantages of spiral devices include simplicity in microfabrication (3D printing is possible [68]), low clogging issues due to large channel dimensions, high separation resolution, and scalability for macro-scale volume processing.

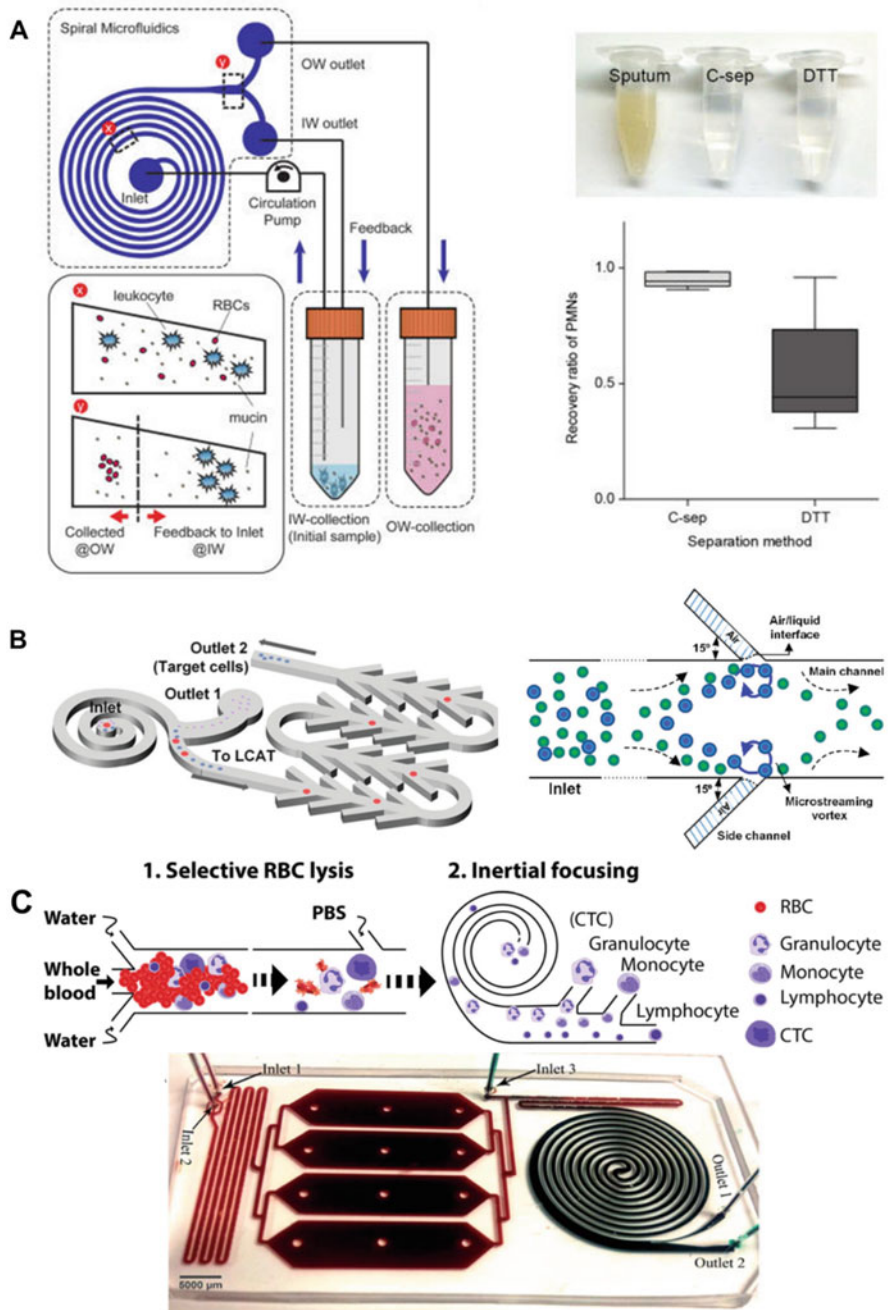


Fig. 5.24 (a) (left) Recirculation spiral microfluidics strategy (right) Images and plots showing sputum and purified samples using their system (C-sep) and DTT protocol. (Reprinted (adapted)

In this chapter, we have provided a comprehensive review on spiral inertial microfluidics and covered related topics including (1) conventional and microfluidic cell sorting techniques, (2) introductory theory in inertial microfluidics and Dean-coupled inertial focusing, (3) classification of major spiral devices, (4) sorting of cells and biomolecules using spiral technologies, and (5) recent advances in next generation spiral cell sorters. Noteworthy, we have also provided tables (in different sections) to highlight key principles and features in different spiral designs, as well as comparing separation performances in various cell-based applications. We believe this broad overview will be invaluable to readers who are new to the topic and keen to use spiral cell sorting technology.

As the spiral inertial microfluidics community continues to grow, there are several important areas that researchers can contribute to enable novel applications and improve understanding on the underlying physics. Being a size-based separation technology, it remains challenging to purify cells of closely-spaced sizes or with other biophysical differences (cell deformability, electrical properties *etc.*). To enhance sorting specificity, it is important to couple spiral inertial microfluidics with other active or passive sorting techniques which exploit other biophysical parameters such as electrical properties (dielectrophoresis), magnetic properties (magnetophoresis) and mechanical properties (acoustophoresis). The biggest challenge is the flowrate mismatch between spiral device and other techniques as high flow conditions commonly used in spiral channels may not be suitable for other sorting techniques. As cell heterogeneity is becoming increasingly appreciated, another major technological improvement is to integrate biosensing capabilities in spiral sorters to facilitate high throughput real-time single cell analysis. If successful, we are confident that these next-generation integrated spiral platforms will be of great significance for biomedical applications and commercialization opportunities.

Finally, improvement in imaging modalities to characterize particle equilibrium positions in 3D at high flowrates can help to elucidate the underlying physical mechanisms and inertial focusing dynamics [148]. A deeper quantitative analysis of particles inertial focusing in spiral channels can also validate simulation studies and machine learning models to optimize spiral designs and enhance separation capabilities. We envision that with increasing advancement in microfabrication and computational techniques, spiral inertial microfluidics will continue to play a leading role in driving biomedical research by enabling novel and tunable separation technologies with more precision and user-defined separation features.

Fig. 5.24 (continued) with permission from Ref. [145]. Copyright (2017) American Chemical Society. (b) (*left*) Schematic of integrated spiral device with sequential lateral cavity acoustic transducer. (*right*) Microstreaming vortices in LCAT channel for particle trapping. (Adapted with permission from Ref. [96]) (c) (*top*) Workflow and image of the integrated spiral device with on-chip RBC lysis. (Reproduced from Ref. [146] – published by The Royal Society of Chemistry, under Creative Commons)

References

1. Antfolk M, Laurell T (2017) Continuous flow microfluidic separation and processing of rare cells and bioparticles found in blood – a review. *Anal Chim Acta* 965:9–35
2. Tomlinson MJ, Tomlinson S, Yang XB, Kirkham J (2013) Cell separation: terminology and practical considerations. *J Tissue Eng* 4:2041731412472690
3. Bhagat AAS, Bow H, Hou HW, Tan SJ, Han J, Lim CT (2010) Microfluidics for cell separation. *Med Biol Eng Comput* 48(10):999–1014
4. Faraghat SA, Hoettges KF, Steinbach MK, van der Veen DR, Brackenbury WJ, Henslee EA et al (2017) High-throughput, low-loss, low-cost, and label-free cell separation using electrophysiology-activated cell enrichment. *Proc Natl Acad Sci* 114(18):4591–4596
5. Gossett DR, Weaver WM, Mach AJ, Hur SC, Tse HT, Lee W et al (2010) Label-free cell separation and sorting in microfluidic systems. *Anal Bioanal Chem* 397(8):3249–3267
6. Manz A, Graber N, Widmer HM (1990) Miniaturized total chemical-analysis systems – a novel concept for chemical sensing. *Sensors Actuators B-Chem* 1(1–6):244–248
7. Lenshof A, Laurell T (2010) Continuous separation of cells and particles in microfluidic systems. *Chem Soc Rev* 39(3):1203–1217
8. Shields CW, Reyes CD, Lopez GP (2015) Microfluidic cell sorting: a review of the advances in the separation of cells from debulking to rare cell isolation. *Lab Chip* 15(5):1230–1249
9. Squires TM, Quake SR (2005) Microfluidics: fluid physics at the nanoliter scale. *Rev Mod Phys* 77(3):977–1026
10. Sajeesh P, Sen AK (2014) Particle separation and sorting in microfluidic devices: a review. *Microfluid Nanofluid* 17(1):1–52
11. Yan S, Zhang J, Yuan D, Li WH (2017) Hybrid microfluidics combined with active and passive approaches for continuous cell separation. *Electrophoresis* 38(2):238–249
12. Berger M, Castelino J, Huang R, Shah M, Austin RH (2001) Design of a microfabricated magnetic cell separator. *Electrophoresis* 22(18):3883–3892
13. Inglis DW, Riehn R, Austin RH, Sturm JC (2004) Continuous microfluidic immunomagnetic cell separation. *Appl Phys Lett* 85(21):5093–5095
14. Pamme N, Wilhelm C (2006) Continuous sorting of magnetic cells via on-chip free-flow magnetophoresis. *Lab Chip* 6(8):974–980
15. Cetin B, Li DQ (2011) Dielectrophoresis in microfluidics technology. *Electrophoresis* 32(18):2410–2427
16. Lenshof A, Magnusson C, Laurell T (2012) Acoustofluidics 8: applications of acoustophoresis in continuous flow microsystems. *Lab Chip* 12(7):1210–1223
17. Ding XY, Peng ZL, Lin SCS, Geri M, Li SX, Li P et al (2014) Cell separation using tilted-angle standing surface acoustic waves. *Proc Natl Acad Sci USA* 111(36):12992–12997
18. MacDonald MP, Spalding GC, Dholakia K (2003) Microfluidic sorting in an optical lattice. *Nature* 426(6965):421–424
19. Yang S, Undar A, Zahn JD (2006) A microfluidic device for continuous, real time blood plasma separation. *Lab Chip* 6(7):871–880
20. Yamada M, Seki M (2005) Hydrodynamic filtration for on-chip particle concentration and classification utilizing microfluidics. *Lab Chip* 5(11):1233–1239
21. Yamada M, Kano K, Tsuda Y, Kobayashi J, Yamato M, Seki M et al (2007) Microfluidic devices for size-dependent separation of liver cells. *Biomed Microdevices* 9(5):637–645
22. Choi S, Song S, Choi C, Park JK (2007) Continuous blood cell separation by hydrophoretic filtration. *Lab Chip* 7(11):1532–1538
23. Kuntaegowdanahalli SS, Bhagat AAS, Kumar G, Papautsky I (2009) Inertial microfluidics for continuous particle separation in spiral microchannels. *Lab Chip* 9(20):2973–2980
24. Davis JA, Inglis DW, Morton KJ, Lawrence DA, Huang LR, Chou SY et al (2006) Deterministic hydrodynamics: taking blood apart. *Proc Natl Acad Sci USA* 103(40):14779–14784

25. Sethu P, Sin A, Toner M (2006) Microfluidic diffusive filter for apheresis (leukapheresis). *Lab Chip* 6(1):83–89
26. Nagrath S, Inglis DW, Morton KJ, Lawrence DA, Huang LR, Chou SY et al (2007) Isolation of rare circulating tumour cells in cancer patients by microchip technology. *Nature* 450(7173):1235–1239
27. Takagi J, Yamada M, Yasuda M, Seki M (2005) Continuous particle separation in a microchannel having asymmetrically arranged multiple branches. *Lab Chip* 5(7):778–784
28. Huang LR, Cox EC, Austin RH, Sturm JC (2004) Continuous particle separation through deterministic lateral displacement. *Science* 304(5673):987–990
29. Yamada M, Nakashima M, Seki M (2004) Pinched flow fractionation: continuous size separation of particles utilizing a laminar flow profile in a pinched microchannel. *Anal Chem* 76(18):5465–5471
30. Di Carlo D, Irimia D, Tompkins RG, Toner M (2007) Continuous inertial focusing, ordering, and separation of particles in microchannels. *Proc Natl Acad Sci USA* 104(48):18892–18897
31. Bhagat AAS, Kuntaegowdanahalli SS, Papautsky I (2008) Continuous particle separation in spiral microchannels using dean flows and differential migration. *Lab Chip* 8(11):1906–1914. <https://doi.org/10.1039/B807107A>
32. Di Carlo D, Edd JF, Humphry KJ, Stone HA, Toner M (2009) Particle segregation and dynamics in confined flows. *Phys Rev Lett* 102(9)
33. Di Carlo D (2009) Inertial microfluidics. *Lab Chip* 9(21):3038–3046
34. Amini H, Lee W, Di Carlo D (2014) Inertial microfluidic physics. *Lab Chip* 14(15):2739–2761
35. Martel JM, Toner M (2014) Inertial focusing in microfluidics. *Annu Rev Biomed Eng* 16:371–396
36. Zhang J, Yan S, Yuan D, Alici G, Nguyen NT, Warkiani ME et al (2016) Fundamentals and applications of inertial microfluidics: a review. *Lab Chip* 16(1):10–34
37. Avila K, Moxey D, de Lozar A, Avila M, Barkley D, Hof B (2011) The onset of turbulence in pipe flow. *Science* 333(6039):192–196
38. Sudarsan AP, Ugaz VM (2006) Multivortex micromixing. *Proc Natl Acad Sci USA* 103(19):7228–7233
39. Segre G, Silberberg A (1961) Radial particle displacements in Poiseuille flow of suspensions. *Nature* 189(476):209–210
40. Segré G, Silberberg A (1962) Behaviour of macroscopic rigid spheres in Poiseuille flow: part 2. Experimental results and interpretation. *J Fluid Mech* 14(1):136–157
41. Asmolov ES (1999) The inertial lift on a spherical particle in a plane Poiseuille flow at large channel Reynolds number. *J Fluid Mech* 381:63–87
42. Dean WR (1928) The stream-line motion of fluid in a curved pipe. (Second paper.). *Philos Mag* 5(30):673–695
43. Ookawara S, Higashi R, Street D, Ogawa K (2004) Feasibility study on concentration of slurry and classification of contained particles by microchannel. *Chem Eng J* 101(1–3):171–178
44. Gossett DR, Di Carlo D (2009) Particle focusing mechanisms in curving confined flows. *Anal Chem* 81(20):8459–8465
45. Saffman PG (1965) The lift on a small sphere in a slow shear flow. *J Fluid Mech* 22(2):385–400
46. Cherukat P, McLaughlin JB (1994) The inertial lift on a rigid sphere in a linear shear flow field near a flat wall. *J Fluid Mech* 263:1–18
47. Loth E, Dorgan AJ (2009) An equation of motion for particles of finite Reynolds number and size. *Environ Fluid Mech* 9(2):187–206
48. Zhou J, Giridhar PV, Kasper S, Papautsky I (2013) Modulation of aspect ratio for complete separation in an inertial microfluidic channel. *Lab Chip* 13(10):1919–1929
49. Zhou J, Papautsky I (2013) Fundamentals of inertial focusing in microchannels. *Lab Chip* 13(6):1121–1132
50. Bhagat AAS, Kuntaegowdanahalli SS, Papautsky I (2008) Enhanced particle filtration in straight microchannels using shear-modulated inertial migration. *Phys Fluids* 20(10):101702

51. Kim TH, Yoon HJ, Stella P, Nagrath S (2014) Cascaded spiral microfluidic device for deterministic and high purity continuous separation of circulating tumor cells. *Biomicrofluidics* 8(6):13. Art. no. 064117
52. Sudarsan AP, Ugaz VM (2006) Fluid mixing in planar spiral microchannels. *Lab Chip* 6(1):74–82
53. Sudarsan AP, Ugaz VM (2006) Multivortex micromixing. *Proc Natl Acad Sci* 103(19):7228–7233
54. Wang J, Zhan Y, Ugaz VM, Lu C (2010) Vortex-assisted DNA delivery. *Lab Chip* 10(16):2057–2061
55. Martel JM, Toner M (2012) Inertial focusing dynamics in spiral microchannels. *Phys Fluids* 24(3):032001
56. Russom A, Gupta AK, Nagrath S, Di Carlo D, Edd JF, Toner M (2009) Differential inertial focusing of particles in curved low-aspect-ratio microchannels. *New J Phys* 11:075025
57. Xiang N, Chen K, Sun D, Wang S, Yi H, Ni Z (2013) Quantitative characterization of the focusing process and dynamic behavior of differently sized microparticles in a spiral microchannel. *Microfluid Nanofluid* 14(1):89–99
58. Kemna EWM, Schoeman RM, Wolbers F, Vermes I, Weitz DA, van den Berg A (2012) High-yield cell ordering and deterministic cell-in-droplet encapsulation using Dean flow in a curved microchannel. *Lab Chip* 12(16):2881–2887
59. Seo J, Lean MH, Kole A (2007) Membrane-free microfiltration by asymmetric inertial migration. *Appl Phys Lett* 91(3):033901
60. Sun J, Li M, Liu C, Zhang Y, Liu D, Liu W et al (2012) Double spiral microchannel for label-free tumor cell separation and enrichment. *Lab Chip* 12(20):3952–3960
61. Sun J, Liu C, Li M, Wang J, Xianyu Y, Hu G et al (2013) Size-based hydrodynamic rare tumor cell separation in curved microfluidic channels. *Biomicrofluidics* 7(1):011802
62. Xi W, Kong F, Yeo JC, Yu L, Sonam S, Dao M et al (2017) Soft tubular microfluidics for 2D and 3D applications. *Proc Natl Acad Sci* 114(40):10590–10595
63. Nivedita N, Ligrani P, Papautsky I (2017) Dean flow dynamics in low-aspect ratio spiral microchannels. *Sci Rep* 7:44072
64. Guan G, Wu L, Bhagat AA, Li Z, Chen PCY, Chao S et al (2013) Spiral microchannel with rectangular and trapezoidal cross-sections for size based particle separation. *Sci Rep* 3:1475
65. Wu L, Guan G, Hou HW, Asgar A, Bhagat S, Han J (2012) Separation of leukocytes from blood using spiral channel with trapezoid cross-section. *Anal Chem* 84(21):9324–9331
66. Warkiani ME, Guan G, Luan KB, Lee WC, Bhagat AAS, Chaudhuri PK et al (2014) Slanted spiral microfluidics for the ultra-fast, label-free isolation of circulating tumor cells. *Lab Chip* 14(1):128–137
67. Warkiani ME, Tay AKP, Guan G, Han J (2015) Membrane-less microfiltration using inertial microfluidics. *Sci Rep* 5:11018
68. Lee W, Kwon D, Choi W, Jung GY, Au AK, Folch A et al (2015) 3D-printed microfluidic device for the detection of pathogenic bacteria using size-based separation in helical channel with trapezoid cross-section. *Sci Rep* 5:7717
69. Hou HW, Bhagat AAS, Lee WC, Huang S, Han J, Lim CT (2011) Microfluidic devices for blood fractionation. *Micromachines* 2(3):319–343
70. Hou HW, Warkiani ME, Khoo BL, Li ZR, Soo RA, Tan DS-W et al (2013) Isolation and retrieval of circulating tumor cells using centrifugal forces. *Sci Rep* 3:1259
71. Vona G, Sabile A, Louha M, Sitruk V, Romana S, Schutze K et al (2000) Isolation by size of epithelial tumor cells – a new method for the immunomorphological and molecular characterization of circulating tumor cells. *Am J Pathol* 156(1):57–63
72. Zabaglo L, Ormerod MG, Parton M, Ring A, Smith IE, Dowsett M (2003) Cell filtration-laser scanning cytometry for the characterisation of circulating breast cancer cells. *Cytometry A* 55(2):102–108

73. Hou HW, Bhattacharyya RP, Hung DT, Han J (2015) Direct detection and drug-resistance profiling of bacteremias using inertial microfluidics. *Lab Chip* 15(10):2297–2307. <https://doi.org/10.1039/C5LC00311C>
74. Birch CM, Hou HW, Han J, Niles JC (2015) Identification of malaria parasite-infected red blood cell surface aptamers by inertial microfluidic SELEX (I-SELEX). *Sci Rep* 5:11347
75. Yeo DC, Wiraja C, Zhou Y, Tay HM, Xu C, Hou HW (2015) Interference-free micro/nanoparticle cell engineering by use of high-throughput microfluidic separation. *ACS Appl Mater Interfaces* 7(37):20855–20864
76. Tay HM, Kharel S, Dalan R, Chen ZJ, Tan KK, Boehm BO et al (2017) Rapid purification of sub-micrometer particles for enhanced drug release and microvesicles isolation. *NPG Asia Mater* 9:e434
77. Sollier E, Murray C, Maoddi P, Di Carlo D (2011) Rapid prototyping polymers for microfluidic devices and high pressure injections. *Lab Chip* 11(22):3752–3765
78. Johnston ID, McDonnell MB, Tan CKL, McCluskey DK, Davies MJ, Tracey MC (2014) Dean flow focusing and separation of small microspheres within a narrow size range. *Microfluid Nanofluid* 17(3):509–518
79. Dong Y, Skelley AM, Merdek KD, Sprott KM, Jiang CS, Pierceall WE et al (2013) Microfluidics and circulating tumor cells. *J Mol Diagn* 15(2):149–157
80. Cristofanilli M, Budd GT, Ellis MJ, Stopeck A, Matera J, Miller MC et al (2004) Circulating tumor cells, disease progression, and survival in metastatic breast cancer. *N Engl J Med* 351(8):781–791
81. Hayes DF, Cristofanilli M, Budd GT, Ellis MJ, Stopeck A, Miller MC et al (2006) Circulating tumor cells at each follow-up time point during therapy of metastatic breast cancer patients predict progression-free and overall survival. *Clin Cancer Res* 12(14):4218–4224
82. Yu L, Ng SR, Xu Y, Dong H, Wang YJ, Li CM (2013) Advances of lab-on-a-chip in isolation, detection and post-processing of circulating tumour cells. *Lab Chip* 13(16):3163–3182
83. Chen P, Huang YY, Hoshino K, Zhang XJ (2014) Multiscale immunomagnetic enrichment of circulating tumor cells: from tubes to microchips. *Lab Chip* 14(3):446–458
84. Hajba L, Guttman A (2014) Circulating tumor-cell detection and capture using microfluidic devices. *Trends Anal Chem* 59:9–16
85. Murlidhar V, Rivera-Baez L, Nagrath S (2016) Affinity versus label-free isolation of circulating tumor cells: who wins? *Small* 12(33):4450–4463
86. Nagrath S, Sequist LV, Maheswaran S, Bell DW, Irimia D, Ulkus L et al (2007) Isolation of rare circulating tumour cells in cancer patients by microchip technology. *Nature* 450(7173):1235–1239
87. Stott SL, Hsu CH, Tsukrov DI, Yu M, Miyamoto DT, Waltman BA et al (2010) Isolation of circulating tumor cells using a microvortex-generating herringbone-chip. *Proc Natl Acad Sci USA* 107(43):18392–18397
88. Sun JS, Liu C, Li MM, Wang JD, Xianyu YL, Hu GQ et al (2013) Size-based hydrodynamic rare tumor cell separation in curved microfluidic channels. *Biomicrofluidics* 7(1):11802
89. Burke JM, Zubajlo RE, Smela E, White IM (2014) High-throughput particle separation and concentration using spiral inertial filtration. *Biomicrofluidics* 8(2):17, Art. no. 024105
90. Khoo BL, Warkiani ME, Tan DSW, Bhagat AAS, Irwin D, Lau DP, et al. (2014) Clinical validation of an ultra high-throughput spiral microfluidics for the detection and enrichment of viable circulating tumor cells. *PLoS One* 9(7):7, Art. no. e99409
91. Warkiani ME, Khoo BL, Tan DS-W, Bhagat AAS, Lim W-T, Yap YS et al (2014) An ultra-high-throughput spiral microfluidic biochip for the enrichment of circulating tumor cells. *Analyst* 139(13):3245–3255. <https://doi.org/10.1039/C4AN00355A>
92. Wang JD, Lu WJ, Tang CH, Liu Y, Sun JS, Mu X et al (2015) Label-free isolation and mRNA detection of circulating tumor cells from patients with metastatic lung cancer for disease diagnosis and monitoring therapeutic efficacy. *Anal Chem* 87(23):11893–11900

93. Huang D, Shi X, Qian Y, Tang WL, Liu LB, Xiang N et al (2016) Rapid separation of human breast cancer cells from blood using a simple spiral channel device. *Anal Methods* 8 (30):5940–5948
94. Warkiani ME, Khoo BL, Wu LD, Tay AKP, Bhagat AAS, Han J et al (2016) Ultra-fast, label-free isolation of circulating tumor cells from blood using spiral microfluidics. *Nat Protoc* 11 (1):134–148
95. Kulasinghe A, Tran THP, Blick T, O'Byrne K, Thompson EW, Warkiani ME et al (2017) Enrichment of circulating head and neck tumour cells using spiral microfluidic technology. *Sci Rep* 7
96. Nivedita N, Garg N, Lee AP, Papautsky I (2017) A high throughput microfluidic platform for size-selective enrichment of cell populations in tissue and blood samples. *Analyst* 142 (14):2558–2569
97. Bhagat AAS, Kuntaegowdanahalli SS, Kaval N, Seliskar CJ, Papautsky I (2010) Inertial microfluidics for sheath-less high-throughput flow cytometry. *Biomed Microdevices* 12 (2):187–195
98. Aya-Bonilla CA, Marsavela G, Freeman JB, Lomma C, Frank MH, Khattak MA et al (2017) Isolation and detection of circulating tumour cells from metastatic melanoma patients using a slanted spiral microfluidic device. *Oncotarget* 8(40):67355–67368
99. Diogo MM, da Silva CL, Cabral JMS (2012) Separation technologies for stem cell bioprocessing. *Biotechnol Bioeng* 109(11):2699–2709
100. Zhu BL, Murthy SK (2013) Stem cell separation technologies. *Curr Opin Chem Eng* 2(1):3–7
101. Machado HL, Kittrell FS, Edwards D, White AN, Atkinson RL, Rosen JM et al (2013) Separation by cell size enriches for mammary stem cell repopulation activity. *Stem Cells Transl Med* 2(3):199–203
102. Davis PK, Ho A, Dowdy SF (2001) Biological methods for cell-cycle synchronization of mammalian cells. *BioTechniques* 30(6):1322–+
103. Choi S, Song S, Choi C, Park JK (1964-1968) Microfluidic self-sorting of mammalian cells to achieve cell cycle synchrony by hydrophoresis. *Anal Chem* 81(5):2009
104. Lee WC, Bhagat AAS, Huang S, Van Vliet KJ, Han J, Lim CT (2011) High-throughput cell cycle synchronization using inertial forces in spiral microchannels. *Lab Chip* 11 (7):1359–1367
105. Lee WC, Shi H, Poon ZY, Nyan LM, Kaushik T, Shivashankar GV et al (2014) Multivariate biophysical markers predictive of mesenchymal stromal cell multipotency. *Proc Natl Acad Sci USA* 111(42):E4409–E4418
106. Nathangari SSP, Dong BQ, Zhou F, Kang WM, Giraldo-Vela JP, McGuire T et al (2015) Isolating single cells in a neurosphere assay using inertial microfluidics. *Lab Chip* 15 (24):4591–4597
107. Song HJ et al (2017) Spiral-shaped inertial stem cell device for high-throughput enrichment of iPSC-derived neural stem cells. *Microfluid Nanofluid* 21(4):1–9
108. Rossi F, Cattaneo E (2002) Opinion – neural stem cell therapy for neurological diseases: dreams and reality. *Nat Rev Neurosci* 3(5):401–409
109. Marshall GP, Reynolds BA, Laywell ED (2007) Using the neurosphere assay to quantify neural stem cells in vivo. *Curr Pharm Biotechnol* 8(3):141–145
110. Deleyrolle LP, Rietze RL, Reynolds BA (2008) The neurosphere assay, a method under scrutiny. *Acta Neuropsychiatrica* 20(1):2–8
111. Alba-Loureiro TC et al (2007) Neutrophil function and metabolism in individuals with diabetes mellitus. *Braz J Med Biol Res* 40(8):1037–1044
112. Gregory AD, Houghton AM (2011) Tumor-associated neutrophils: new targets for cancer therapy. *Cancer Res* 71(7):2411–2416
113. Papa A, Emdin M, Passino C, Michelassi C, Battaglia D, Cocci F (2008) Predictive value of elevated neutrophil-lymphocyte ratio on cardiac mortality in patients with stable coronary artery disease. *Clin Chim Acta* 395(1–2):27–31

114. Ernst E, Matrai A (1986) Altered red and white blood-cell rheology in type-ii diabetes. *Diabetes* 35(12):1412–1415
115. Pecsvarady Z, Fisher TC, Darwin CH, Fabok A, Maqueda TS, Saad MF et al (1994) Decreased polymorphonuclear leukocyte deformability in Niddm. *Diabetes Care* 17(1):57–63
116. Mowat AG, Baum J (1971) Chemotaxis of polymorphonuclear leukocytes from patients with diabetes mellitus. *N Engl J Med* 284(12):621–627
117. Delamaire M, Maugendre D, Moreno M, LeGoff MC, Allannic H, Genetet B (1997) Impaired leucocyte functions in diabetic patients. *Diabet Med* 14(1):29–34
118. Bagdade JD, Root RK, Bulger RJ (1974) Impaired leukocyte function in patients with poorly controlled diabetes. *Diabetes* 23(1):9–15
119. Hou HW, Petchakup C, Tay HM, Tam ZY, Dalan R, Chew DEK et al (2016) Rapid and label-free microfluidic neutrophil purification and phenotyping in diabetes mellitus. *Sci Rep* 6
120. Nivedita N, Papautsky I (2013) Continuous separation of blood cells in spiral microfluidic devices. *Biomicrofluidics* 7(5):54101
121. Agarwal A, Ikemoto I, Loughlin KR (1994) Effect of sperm washing on levels of reactive oxygen species in semen. *Arch Androl* 33(3):157–162
122. Swain JE, Lai D, Takayama S, Smith GD (2013) Thinking big by thinking small: application of microfluidic technology to improve ART. *Lab Chip* 13(7):1213–1224
123. Son JY, Murphy K, Samuel R, Gale BK, Carrell DT, Hotaling JM (2015) Non-motile sperm cell separation using a spiral channel. *Anal Methods* 7(19):8041–8047
124. Hou HW, Gan HY, Bhagat AAS, Li LD, Lim CT, Han J (2012) A microfluidics approach towards high-throughput pathogen removal from blood using margination. *Biomicrofluidics* 6(2):24115
125. Schaap A, Dumon J, den Toonder J (2016) Sorting algal cells by morphology in spiral microchannels using inertial microfluidics. *Microfluid Nanofluid* 20(9):125
126. Clime L, Li K, Geissler M, Hoa XD, Robideau GP, Bilodeau GJ, et al (2017) Separation and concentration of *Phytophthora ramorum* sporangia by inertial focusing in curving microfluidic flows. *Microfluid Nanofluid* 21(1):13 Art. no. 5
127. Schets FA, van Wijnen JH, Schijven JF, Schoon A, Husmant A (2008) Monitoring of waterborne pathogens in surface waters in Amsterdam, The Netherlands, and the potential health risk associated with exposure to *Cryptosporidium* and *Giardia* in these waters. *Appl Environ Microbiol* 74(7):2069–2078
128. Bridle H, Kersaudy-Kerhoas M, Miller B, Gavriilidou D, Katzer F, Innes EA et al (2012) Detection of *Cryptosporidium* in miniaturised fluidic devices. *Water Res* 46(6):1641–1661
129. Jimenez M, Miller B, Bridle HL (Jan 2017) Efficient separation of small microparticles at high flowrates using spiral channels: application to waterborne pathogens. *Chem Eng Sci* 157:247–254
130. Sarkar A, Hou HW, Mahan AE, Han J, Alter G (2016) Multiplexed affinity-based separation of proteins and cells using inertial microfluidics. *Sci Rep* 6
131. Cheung YW, Dirkwager RM, Wong WC, Cardoso J, D’Arc Neves Costa J, Tanner JA (2017) Aptamer-mediated Plasmodium-specific diagnosis of malaria. *Biochimie*. in press
132. Tuerk C, Gold L (1990) Systematic evolution of ligands by exponential enrichment: RNA ligands to bacteriophage T4 DNA polymerase. *Science* 249(4968):505–510
133. Ellington AD, Szostak JW (1990) In vitro selection of RNA molecules that bind specific ligands. *Nature* 346(6287):818–822
134. Berezovski M, Drabovich A, Krylova SM, Musheev M, Okhonin V, Petrov A et al (2005) Nonequilibrium capillary electrophoresis of equilibrium mixtures: a universal tool for development of aptamers. *J Am Chem Soc* 127(9):3165–3171
135. Sonmez U, Jaber S, Trabzon L (2017) Super-enhanced particle focusing in a novel microchannel geometry using inertial microfluidics. *J Micromech Microeng* 27(6):065003
136. Hahn Y, Hong D, Kang J, Choi S (2016) A reconfigurable microfluidics platform for microparticle separation and fluid mixing. *Micromachines* 7(8):139

137. Geng Z, Ju Y, Wang W, Li Z (2013) Continuous blood separation utilizing spiral filtration microchannel with gradually varied width and micro-pillar array. *Sensors Actuators B Chem* 180:122–129
138. Ghadami S, Kowsari-Esfahan R, Saidi MS, Firozabakhsh K (2017) Spiral microchannel with stair-like cross section for size-based particle separation. *Microfluid Nanofluid* 21(7):115
139. Shen S, Tian C, Li T, Xu J, Chen S-W, Tu Q et al (2017) Spiral microchannel with ordered micro-obstacles for continuous and highly-efficient particle separation. *Lab Chip*. <https://doi.org/10.1039/C7LC00691H>
140. Khoo BL, Warkiani ME, Tan DS, Bhagat AA, Irwin D, Lau DP et al (2014) Clinical validation of an ultra high-throughput spiral microfluidics for the detection and enrichment of viable circulating tumor cells. *PLoS One* 9(7):e99409
141. Miller B, Jimenez M, Bridle H (2016) Cascading and parallelising curvilinear inertial focusing systems for high volume, wide size distribution, separation and concentration of particles. *Sci Rep* 6:36386
142. Rafeie M, Zhang J, Asadnia M, Li W, Warkiani ME (2016) Multiplexing slanted spiral microchannels for ultra-fast blood plasma separation. *Lab Chip* 16(15):2791–2802. <https://doi.org/10.1039/C6LC00713A>
143. Kwon T, Prentice H, Oliveira JD, Madziva N, Warkiani ME, Hamel J-FP et al (2017) Microfluidic cell retention device for perfusion of mammalian suspension culture. *Sci Rep* 7(1):6703
144. Robinson M, Marks H, Hinsdale T, Maitland K, Cote G (2017) Rapid isolation of blood plasma using a cascaded inertial microfluidic device. *Biomicrofluidics* 11(2):024109
145. Ryu H, Choi K, Qu Y, Kwon T, Lee JS, Han J (2017) Patient-derived airway secretion dissociation technique to isolate and concentrate immune cells using closed-loop inertial microfluidics. *Anal Chem* 89(10):5549–5556
146. Ramachandraiah H, Svahn HA, Russom A (2017) Inertial microfluidics combined with selective cell lysis for high throughput separation of nucleated cells from whole blood. *RSC Adv* 7(47):29505–29514. <https://doi.org/10.1039/C7RA02992F>
147. Seo J, Lean MH, Kole A (2007) Membraneless microseparation by asymmetry in curvilinear laminar flows. *J Chromatogr A* 1162(2):126–131
148. Goda K, Ayazi A, Gossett DR, Sadasivam J, Lonappan CK, Sollier E et al (2012) High-throughput single-microparticle imaging flow analyzer. *Proc Natl Acad Sci* 109(29):11630–11635